Correspondence to:
L. T. Bach,
lennart.bach@utas.edu.au

The Influence of Plankton Community Structure on Sinking Velocity and Remineralization Rate of Marine Aggregates

L. T. Bach[1,2] , P. Stange[2] , J. Taucher[2] , E. P. Achterberg[2], M. Algueró-Muñiz[3], H. Horn[4], M. Esposito[2], and U. Riebesell[2]

[1]Institute for Marine and Antarctic Studies, University of Tasmania, Hobart, Tasmania, Australia, [2]GEOMAR Helmholtz Centre of Ocean Research Kiel, Kiel, Germany, [3]Alfred-Wegener-Institut Helmholtz-Zentrum für Polar- und Meeresforschung, Biologische Anstalt Helgoland, Helgoland, Germany, [4]NIOZ Royal Netherlands Institute for Sea Research and Utrecht University, Yerseke, The Netherlands

Abstract Gravitational sinking of photosynthetically fixed particulate organic carbon (POC) constitutes a key component of the biological carbon pump. The fraction of POC leaving the surface ocean depends on POC sinking velocity (SV) and remineralization rate (C_{remin}), both of which depend on plankton community structure. However, the key drivers in plankton communities controlling SV and C_{remin} are poorly constrained. In fall 2014, we conducted a 6-week mesocosm experiment in the subtropical NE Atlantic Ocean to study the influence of plankton community structure on SV and C_{remin}. Oligotrophic conditions prevailed for the first 3 weeks, until nutrient-rich deep water injected into all mesocosms stimulated diatom blooms. SV declined steadily over the course of the experiment due to decreasing $CaCO_3$ ballast and—according to an optical proxy proposed herein—due to increasing aggregate porosity mostly during an aggregation event after the diatom bloom. Furthermore, SV was positively correlated with the contribution of picophytoplankton to the total phytoplankton biomass. C_{remin} was highest during a *Synechococcus* bloom under oligotrophic conditions and in some mesocosms during the diatom bloom after the deep water addition, while it was particularly low during harmful algal blooms. The temporal changes were considerably larger in C_{remin} (max. fifteenfold) than in SV (max. threefold). Accordingly, estimated POC transfer efficiency to 1,000 m was mainly dependent on how the plankton community structure affected C_{remin}. Our approach revealed key players and interactions in the plankton food web influencing POC export efficiency thereby improving our mechanistic understanding of the biological carbon pump.

1. Introduction

Phytoplankton fix approximately 50-Gt carbon per year, which is comparable to the annual primary production of the terrestrial biosphere (Field et al., 1998; Longhurst et al., 1995). The majority of the organic biomass generated by phytoplankton is consumed and remineralized in the surface ocean, while 11–27% is exported below the euphotic zone (Field et al., 1998; Henson et al., 2011). This export flux maintains a permanent surface-to-depth CO_2 gradient, which allows the ocean to store significantly more atmospheric CO_2 than it would without this biological carbon pump (BCP; Volk & Hoffert, 1985). The BCP is driven by (1) gravitational sinking of particulate organic carbon (POC), (2) downwelling of POC and dissolved organic carbon (DOC), and (3) zooplankton-mediated active transport (Ducklow et al., 2001; Hansell & Carlson, 2001; Steinberg et al., 2008). Among these mechanisms, gravitational sinking is considered the most important pathway, although this is still a matter of debate (Boyd et al., 2019; Hernández-León et al., 2019; Steinberg & Landry, 2017; Stukel et al., 2018).

The efficiency of the BCP through gravitational sinking can be determined empirically by fitting a power law function to, for example, depth-resolved sediment trap fluxes (Martin et al., 1987). This provides the *b* value, which quantifies the transfer efficiency from the surface to the deep ocean. However, it is also possible to determine BCP efficiency mechanistically by assessing the ratio of carbon-specific remineralization rates (C_{remin} in d^{-1}) and particle sinking velocity (SV in $m\ d^{-1}$; Sanders et al., 2014). This ratio is known as the remineralization length scale (RLS in m^{-1}) and quantifies the fraction of carbon within an aggregate that is remineralized per meter sinking (e.g., Belcher et al., 2016; Iversen et al., 2010). Densely packed and heavily ballasted particles will sink rapidly and provide relatively little surface area for bacterial remineralization

(low RLS). Conversely, fluffy aggregates with plentiful easily degradable organic matter will sink slowly and be largely decomposed before they reach depths below the winter mixed layer (high RLS; Francois et al., 2002). Assessing the fraction of POC transferred below winter mixed layer depth is important because particles that successfully carry POC down there will likely lock CO_2 in water masses, which have no exchange with the atmosphere for centuries to millennia (Kwon et al., 2009). Both SV and C_{remin} are determined by surface ocean plankton communities as they form the sinking POC and set its initial properties although SV and C_{remin} are modified in deeper water (Fischer & Karakaş, 2009; Henson, Sanders, et al., 2012; Lam et al., 2011; Laurenceau-Cornec et al., 2015; Lomas et al., 2010).

Observations based on sediment trap deployments led to the hypothesis that the availability of ballast minerals largely controls the transfer of POC through the mesopelagic (Armstrong et al., 2002; Francois et al., 2002; Klaas & Archer, 2002). However, more recent assessments of sediment trap data challenged the *ballast ratio hypothesis* (Armstrong et al., 2009) by indicating that the global correlation between ballast and POC fluxes is an artifact of the large degree of spatial averaging (Wilson et al., 2012). Deviations from this correlation exist regionally, indicating that ballast can be very important under certain conditions but other factors such as particle (re)packaging and POC refractiveness against remineralization should also be taken into account to fully understand regionally and temporally changing patterns of CO_2 sequestration efficiency through gravitational sinking (Boyd & Trull, 2007; Le Moigne et al., 2016; Passow & De La Rocha, 2006; Wilson et al., 2012). Particle properties that determine SV and C_{remin} are largely controlled by the plankton community, and therefore, it is essential to understand the ecological processes that form and reprocess sinking POC (Bach et al., 2016; Henson, Lampitt, et al., 2012; Herndl & Reinthaler, 2013; De La Rocha & Passow, 2007; Lam et al., 2011; Lam & Bishop, 2007; Siegel et al., 2014).

However, investigating the links between surface ocean plankton communities and POC exported to depth faces several problems. These are primarily related to the lateral advection of POC during sinking and the time lag between primary production and export. Both must be taken into account to correctly link particles collected at depth with the plankton communities that actually produced them (Henson et al., 2015; Prahl et al., 2000; Stange et al., 2017). In situ mesocosms have been suggested as an important tool to overcome the spatial and temporal challenges associated with oceanic sampling (Bach et al., 2016; Legendre et al., 2018; Sanders et al., 2014). Although mesocosms largely exclude the physical complexity of the marine realm, they enclose the same plankton communities for long times and therefore simulate a Lagrangian system. This allows us to link processes in the plankton community with export-relevant parameters without the ambiguity caused by unconstrained advection or unknown time lags. Indeed, previous in situ mesocosm experiments have proven to be useful for this purpose (Bach et al., 2016; Bressac et al., 2014; Gazeau et al., 2017; Knapp et al., 2016; Stange et al., 2018).

In a recent in situ mesocosm experiment at the Norwegian coast, we investigated the influence of processes in the plankton community on SV (Bach et al., 2016). We found that enhanced ballasting of particulate organic matter by minerals did not necessarily lead to faster sinking of particles. Instead, aggregate porosity played an equally important role, which in turn was dependent on the trophic state of the food web. These results support the notion that plankton community structure is important in controlling SV. However, SV is only one side of the coin and to assess the influence of plankton on BCP efficiency, it is essential to measure SV and C_{remin} simultaneously. We therefore conducted an in situ mesocosm experiment in the oligotrophic NE Atlantic where these two measurements and a detailed examination of the plankton community were combined.

2. Material and Methods

2.1. Experimental Design

On 29 September 2014, we deployed nine units of the Kiel Off-Shore Mesocosms for Future Ocean Simulations (M1–M9; Riebesell et al., 2013) in Gando Bay, Gran Canaria (27°55′41″N, 15°21′55″W). The mesocosms consisted of a cylindrical bag made of transparent polyurethane foil (13 m long, 2 m in diameter), which was suspended in an 8-m high floatation frame. Each bag was equipped with a 2-m-long funnel-shaped sediment trap (Boxhammer et al., 2016).

The mesocosm bags were initially folded to ease their handling. After deployment of the mesocosms in Gando Bay with Research Vessel *Hesperides*, the mesocosm bags were unfolded thereby enclosing ~35 m^3 of seawater. The upper and lower openings of the bags were covered with meshes (3-mm mesh size) during deployment to exclude patchily distributed nekton (e.g., fish) and large zooplankton (e.g., large jelly fish) from the enclosed water mass. The mesocosm bags were left open (with meshes attached) for 4 days to allow rinsing of the mesocosm walls and to ensure homogenous mixing of the water column inside the bags. On 27 September, divers removed the meshes from the openings and attached the sediment traps to the bottom of the mesocosms. The upper ends of the mesocosm bags were pulled above surface on day −4 thereby isolating the water mass. This marked the beginning of the experiment.

Between days 0–6 and on days 21 and 38, seven of the nine mesocosm units were enriched with CO_2 aerated seawater to reach pCO_2 values of 369, 352 (M1 and M9 both untreated control mesocosms), 563 (M3), 668 (M7), 716 (M4), 887 (M2), and 1,025 (M8) μatm. The influence of pCO_2 on SV and C_{remin} was not further explored in our analyses because of three reasons. First, our initial data exploration indicated no clear CO_2 effect. Second, pCO_2 cannot influence SV directly because sinking is a physical process, although it can influence SV by changing plankton communities (Bach et al., 2016). Third, C_{remin} can be influenced directly by pCO_2 by changing metabolic rates of heterotrophs (Piontek et al., 2010) but also by changing plankton communities (Stange et al., 2018). Our setup does not allow us to distinguish this *physiological* from the *ecological* component, but we would expect a much more consistent CO_2 dependency if physiology had been the dominant factor. We therefore focus in this paper on the links between plankton communities and SV and C_{remin} as they seem to be more important, and the findings are also applicable in a more general context (such as coupling ecological processes with export fluxes). Please note, however, that we investigated the influence of pCO_2 on export mass fluxes and organic matter stoichiometry in a separate paper (Stange et al., 2018).

On day 23 we collected ~85 m^3 of natural nutrient-rich seawater from a depth of 650 m with a specifically designed *deep water collection bag*. The bag was lowered to the target depth at a location 4 nautical miles offshore Gran Canaria, where the ocean is ~1,000-m deep, and filled with a remote-controlled propeller system. Once the bag was full, a 300-kg weight was released so that floatation panels mounted at the top of the bag brought it back to the surface. Afterward, the bag was gently towed to the mesocosm deployment site with the vessel SAPCAN IV and moored next to the mesocosms. About 20% (~7 m^3) of the water was pumped out from each mesocosm and replaced with deep water, which was injected evenly into the water columns of the mesocosms with a specifically designed distribution device during the night from day 24 to 25. Please note that mesocosm 6 was irreparably damaged on day 26 and therefore only included in the analyses until that day. A detailed description of all technical operations is provided in the overview paper accompanying this mesocosm campaign (Taucher et al., 2017).

2.2. Sampling and Sample Processing of Water Column Parameters

Suspended particulate material and nutrients in the mesocosm water columns were sampled with two different devices every other day between 09:00 a.m. and 12:00 p.m. from small boats. Chlorophyll *a* (chl-*a*), PM, and phytoplankton were sampled with a specifically designed vacuum pumping system, which efficiently collected equal amounts of water from each depth between 0 and 13 m (Taucher et al., 2017). Nutrient and microzooplankton samples were collected with depth-integrating water samplers (IWSs, Hydro-Bios, Kiel). The IWSs are equipped with pressure sensors and gently take in a total volume of 5 L uniformly distributed over 0–13 m.

Seawater collected with the vacuum system was stored in 20-L carboys and transferred into a temperature-controlled room (set to 15 °C) immediately after arriving at the land-based laboratory facilities of Plataforma Oceánica de Canarias (PLOCAN), which is located next to Taliarte harbor and hosted our study. The 20-L carboys were gently mixed before taking subsamples for the individual measurements. Subsamples for chl-*a* and POC were filtered (Δpressure = 200 mbar) on glass fiber filters (GF/F nominal pore size = 0.7 μm). Chl-*a* samples were immediately frozen to −80 °C and later analyzed using reverse-phase high-performance liquid chromatography following van Heukelem and Thomas (2001). POC filters were stored in glass Petri dishes and immediately frozen to −20 °C after filtration. POC samples were fumed in hydrochloric acid (37%) for 2 hr before measurement. POC concentrations were determined using an elemental analyzer (EuroEA) following Sharp (1974). Flow cytometry subsamples were taken directly from the 20-L

carboys and measured within 3 hr using an Accuri C6 flow cytometer (BD Biosciences). Gates were set based on the forward scatter (FSC-A) and red fluorescence (FL3-A) signals except for the *Synechococcus* group where the orange (FL2-H) instead of FL3-A signal was used to distinguish them from bulk phytoplankton. The size of different phytoplankton groups was determined by fractionation with a variety of polycarbonate filters (0.2, 0.8, 2, 3, 5, and 8 μm) following Veldhuis and Kraay (2000). We distinguished between picoeukaryotes (Peuks; 0.2−2 μm), *Synechococcus*-like autotrophs (*Synechococcus*; 0.6−2 μm), small nanoautotrophs (Nano I; 2−5 μm), larger nanoautotrophs (Nano II; 5−8 μm), and microautotrophs (Micro; >8 μm). We then calculated the relative red fluorescence contribution of each of these groups to the total red fluorescence as described by Bach et al. (2018). A significant linear correlation between FL3-A and chl-*a* concentration confirmed that the red fluorescence measurement is a useful proxy for chl-*a* (Figure S1 in the supporting information). Accordingly, FL3-A was converted to chl-*a* and used thereafter to calculate the percentage each of the above mentioned groups contributed to the total chl-*a* concentration. Samples for transparent exopolymer particles (TEP) were filtered onto polycarbonate filters (0.4-μm pore size) and subsequently stained with Alcian Blue (Passow & Alldredge, 1995). TEP concentrations were determined colorimetrically with a spectrophotometer through absorption at 787 nm. The dye solution had previously been calibrated using Gum Xanthan, and the concentrations of TEP are expressed as microgram Gum Xanthan equivalents per liter (μg GX_{eq} L^{-1}).

IWS microzooplankton samples were transferred into brown glass bottles (250 ml), preserved with acidic Lugol's solution (1–2% final concentration), and stored in the dark until measurement. Abundances of the major groups, that is, ciliates and heterotrophic dinoflagellates, were determined using a Zeiss Axiovert 25 inverse light microscope (Utermöhl, 1958). Seawater collected with the IWS for nutrients were transferred into acid-cleaned (10% HCl) plastic bottles (Series 310 PETG) and filtered using 0.45-μm filters (cellulose acetate, Whatman) directly after arrival at PLOCAN. $NO_3^- + NO_2^-$ (NO_x^-), Si $(OH)_4$, and PO_4^{3-} concentrations were determined photometrically (Hansen & Koroleff, 1999; Murphy & Riley, 1962), while NH_4^+ concentrations were determined fluorometrically (Holmes et al., 1999). The applied analytical tools and specifications to analytical procedures are described with more detail by Taucher et al. (2017).

Mesozooplankton samples were collected every eighth day (2 to 4 p.m. local time) with vertical net hauls using an Apstein net (55-μm mesh size, 17-cm diameter opening) equipped with a closed cod end. The sampling depth was restricted to 13 m to avoid contact of the net with the sediment trap material accumulating at the bottom of the mesocosms. Samples were rinsed on board the sampling boats, collected in containers, and stored in cool boxes until arrival at PLOCAN. Back in the laboratories, samples were preserved in denatured ethanol and quantified and classified to the lowest possible taxonomic level using a stereomicroscope (Olympus SZX9) as described by Algueró-Muñiz et al. (2019)

In situ sizes of aggregates were measured inside the mesocosms with vertical casts of the profiling underwater camera system KIELVISION (Taucher et al., 2018). The camera is equipped with a 12 megapixel sensor, has a resolution of 25 μm per pixel, and photographs a volume of 120 ml per picture. Camera profiles were obtained by manually lowering the system at ~0.5 m/s and recording images from downcasts only. Image acquisition was triggered by an integrated pressure sensor, which was set to obtain one image frame per 0.1-m depth interval, resulting in a total sample volume of ~13–14 L per mesocosm profile. A detailed description of the camera system and the evaluation procedures is provided in the paper by Taucher, Arístegui, et al. (2018).

2.3. Sampling and Processing of Sedimented Particulate Organic Matter

Particulate matter (PM) that settled into the terminal sediment traps at the bottom of the mesocosms was recovered every other day between 08:00 and 09:00 a.m. with the vacuum method described by Boxhammer et al. (2016). Briefly, the collection cylinder at the bottom of the sediment trap was connected to the surface with silicon hose. By applying a weak vacuum to the hose, we sucked all material accumulated in the sediment traps up to the surface and collected this in 5-L glass bottles (Schott Duran). The bottles were stored in cool boxes filled with seawater until arrival in the laboratories at PLOCAN in the early afternoon. Back on shore, we homogenized the samples by gently rotating the glass bottles and took a 60-ml subsample (1–5% of the total sample) with a serological pipette for the determination of SV and C_{remin} (see sections 2.4 and 2.5). The remaining particle suspension was concentrated by centrifugation, freeze-dried, and ground with a ball mill to transform the sample into a homogenous powder (Boxhammer et al., 2016). Total

particulate carbon, nitrogen and phosphorus (TPC, TPN, and TPP), POC, and biogenic silica (BSi) were determined on the powder as described in the following.

For the determination of TPC, TPN, and POC, duplicate subsamples (2 mg) of the sediment powder were transferred into tin (TPC and TPN) or silver cups (POC). POC subsamples were acidified for 1 hr with 1 M HCl and dried at 50 °C overnight. TPC, TPN, and POC concentrations were determined with an elemental analyzer (Euro EA-CN, Hekatech), which was calibrated with acetanilide (C_8H_9NO) and a soil standard (Hekatech, catalogue number HE33860101) prior to each measurement run. Particulate inorganic carbon (PIC) was calculated by subtraction of POC from TPC. For the analysis of BSi, subsamples of 1 mg were transferred into 40-ml plastic vials and heated for 135 min with NaOH (0.1 M) at 85 °C. Subsequently, samples were neutralized using H_2SO_4 (0.05 Molar) and analyzed spectrophotometrically following Hansen and Koroleff (1999).

We typically report PM mass flux to the sediment trap in μmol/L per 48 hr ($G_{measured}$) as this value is useful to calculate elemental budgets and can be easily calculated from known PM mass flux to the sediment traps and mesocosm volumes (Boxhammer et al., 2018). Here, we report PM mass flux in mmol/m^2 per 48 hr (G_{cor}) as this is more easily comparable to the sediment trap and thorium literature (Buesseler, 1998; Honjo et al., 2008). The problem here is that the mesocosm volume varied between 30.8 and 36.8 m^3 because of the flexible nature of the bags even though the diameter of the stabilizing rings was identical (2 m). Thus, to correct the mass flux, we had to normalize the measured mass flux to the average mesocosm volume ($V_{average}$) as

$$G_{cor} = G_{measured} \times V_{mesocosm} \times \frac{V_{mesocosm}}{V_{average}} / \pi r^2 \tag{1}$$

where $V_{mesocosm}$ are the individual volumes of the nine mesocosms determined as described by Taucher et al. (2017) and r is the radius of the cylindrical mesocosm bags (1 m).

2.4. Measurement of Carbon-Specific Remineralization Rates (C_{remin})

Seawater used for dissolved oxygen (O_2) consumption assays was collected from each mesocosm with IWS hauls on days 11, 19, 23, 29, 33, 37, 41, 47, and 53. Samples from each mesocosm were filled headspace-free (allowing significant overflow) into seven 250-ml Schott Duran bottles. No mesh was applied during the filling procedure. The 63 bottles per sampling day were stored in dark plastic boxes and covered with aluminum foil inside cool boxes. Upon arrival in the laboratory (~3–6 hr after taking the samples), all bottles were transferred into a water bath at in situ temperature (22 °C) and stored there in the dark for max. 2 hr until the incubation assays started.

To initiate the incubations, we added 1–3 ml of the PM suspension collected in sediment traps into four of the seven bottles per mesocosm. Unlike in previous experiments (e.g., Bach et al., 2016), the suspension was homogeneous so that 1–3 ml were representative for the bulk sample. The three remaining bottles per mesocosms were not enriched with sediment trap material and served as blank incubations to correct for the O_2 consumption in the natural unfiltered seawater. Care was taken to exclude air bubbles from the incubations. All bottles were placed on a slowly rotating plankton wheel (~1 rpm) and incubated in the dark for up to 39 hr in a temperature-controlled room set to the in situ temperature (22 °C) of surface water (0–15 m) in Gando Bay.

O_2 consumption inside the bottles was measured using noninvasive O_2 sensitive microsensor spots (PSt3-NAU spots, PreSens) mounted with silicon glue inside the 250-ml incubation bottles. The applied sensor spots were two-point calibrated with air-saturated and anoxic water. They had a measurement range of 0–1,400 μmol/L O_2, a resolution of ± 1.4 μmol/L O_2 at 283 μmol/L O_2, and a response time of <40 s. The O_2 concentrations were read 6–7 times during each incubation through the glass walls of the bottles using a handheld optical O_2 meter (Fibox 4, PreSens, Germany). The first measurement was always conducted immediately after the addition of PM to the replicate bottles. The second measurement was taken approximately 2 hr after the start to have a second measurement early during the assay. Subsequent measurements were performed in 8-hr intervals. The Fibox4 handheld O_2 meter automatically corrects for salinity and temperature. We used the daily average salinity determined with a conductivity, temperature, depth (CTD)

AGU
100
ADVANCING EARTH
AND SPACE SCIENCE

Global Biogeochemical Cycles

10.1029/2019GB006256

probe on the day of incubation (Taucher et al., 2017). Temperature was measured in a dummy bottle that was treated similar to the incubation bottles.

After the incubation period, the entire content of the bottles was filtered (Δpressure = 200 mbar) onto combusted glass fiber filters (pore size 0.7, GF/F, Whatman). All filters were fumed with hydrochloric acid (37%) for 2 hr to remove inorganic carbon and dried at 50 °C overnight. POC on these filters was determined as described in section 2.3. The O_2 consumption in each bottle was calculated with linear regressions fitted to the decline in O_2 concentrations over time (Figure S2). The mean O_2 consumption rate measured in the three control bottles (which contained mesocosm water but without the addition of sediment trap material) was subtracted from the O_2 consumption measured in the bottles including sediment trap material (Figure S2). Great care was taken to add sufficient sediment trap material to measure a detectable O_2 consumption over time but at the same time avoid more than ~20 % O_2 consumption during the incubation. Minimizing concentration changes in the course of the incubation is important because the O_2 concentrations itself has an influence on the measured rate (Holtappels et al., 2014; Ploug & Bergkvist, 2015). O_2 consumption rates ($\mu mol \cdot O_2 \cdot L \cdot day$) were converted to CO_2 production rates ($\mu mol \cdot C \cdot L \cdot day$) assuming a widely used respiratory quotient (RQ) of 1-mol O_2 consumed: 1-mol CO_2 produced (Belcher et al., 2016; Cavan & Boyd, 2018; Iversen & Ploug, 2013; Ploug & Grossart, 2000). The C-specific remineralization rate (C_{remin} in d^{-1}) was calculated as

$$C_{remin} = \frac{(r_{sediment} - r_{control})RQ}{POC_{inc}}$$

(2)

where POC_{inc} is the POC content ($\mu mol \cdot C \cdot L$) measured in the incubation bottles and $r_{sediment}$ and $r_{control}$ are the O_2 consumption rates in the bottles with and without sediment trap material, respectively (Figure S2). We approximated the relative uncertainty involved in the C_{remin} bioassay to be ~$\pm$35% based on an error propagation applying the following individual uncertainties: $\pm$20% for RQ based on assessments by (Berggren et al., 2012); $\pm$10% for POC_{inc} based on our experience with sampling and measurement errors associated with elemental analysis; and $\pm$20% for $r_{sediment}$ and $r_{control}$, respectively, based on the approximate variation among replicates (Figure S2).

2.5. Measurement of SV

SV and optical properties of sinking particles recovered from the sediment traps were measured with a FlowCam as described in the method paper by Bach et al. (2012). Briefly, the sediment trap subsample was transferred with pipettes into a settling chamber (1 × 1 cm), which was vertically mounted in the FlowCam. We used a larger settling chamber compared to earlier studies (Bach et al., 2016), to enable the measurements of particles with a maximum equivalent spherical diameter (ESD) of 1,000 μm (with the earlier setup we were restricted to maximally 400 μm). Sinking particles were recorded individually at in situ temperatures of 22 °C for 20 min. The settling chamber was ventilated with a small fan to avoid convection through heat accumulation near the FlowCam electronics.

SV and optical properties recorded with the FlowCam were extracted from the raw data with the MATLAB script described by Bach et al. (2012). For the analysis of SV and particle properties, all particles were grouped into six classes according to their ESD (40–90 μm, 80–130 μm, 120–180 μm, 170–260 μm, 240–400 μm, and 380–1,000 μm). The overlap between classes was necessary in order to avoid exclusion of particles exactly on the borders (Bach et al., 2012). Particles out of focus were removed from the analyses based on their edge gradient. The uncertainty of the mean SV was estimated to be $\pm$15% based on our experience with replicate measurements (Bach et al., 2012).

2.6. Using Optical Properties as a Proxy for Particle Porosity

The FlowCam records 46 optical properties for each particle among which the ESD and *particle intensity* (*Int*) were useful to estimate porosity. ESD is a commonly used metric to assess the diameter of nonspherical particles (Stemmann & Boss, 2012). The FlowCam calculates the ESD as the average of 36 perpendicular distances between parallel tangents touching opposite sides of the particle. *Int* is defined as the grayscale sum divided by the number of pixels making up the particle. *Int* can range between 0 and 255 where higher numbers depict brighter particles. The underlying assumption of our porosity approximation is that aggregates have a higher *Int* in a back-light-illuminated system like the FlowCam (i.e., they appear brighter) when
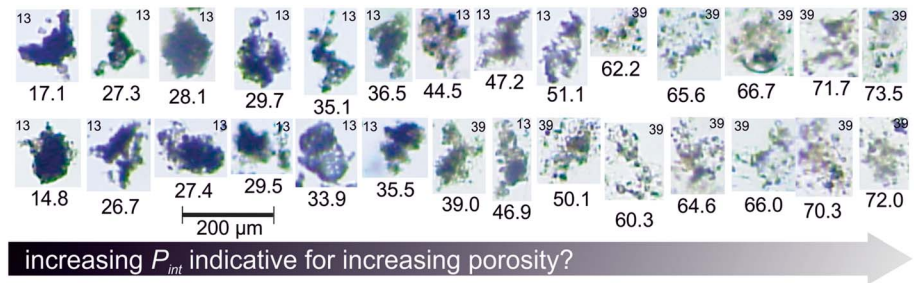
Figure 1. P_{int}, our proxy for aggregate porosity, can be considered as a size-normalized measure of particle intensity (equation (3)) where intensity reflects particle transparency. Shown here are randomly taken FlowCam pictures of sinking particles collected in M3 during two sampling days (days 13 and 39 as noted on each picture at the top). The associated P_{int} values (dimensionless) are given below each picture. P_{int} is higher when the particles are brighter and more transparent, which should be indicative for increased particle porosity (i.e., lower compactness). Low P_{int} particles on the left side of the figure were produced under oligotrophic conditions (day 13), while high P_{int} particles on the right were collected during the mass flux event (day 39).

more of the light passes through the photographed aggregate. This should be the case when the aggregate is porous and relatively little solid matter attenuates the light beam (Figure 1). However, light attenuation also scales with ESD of the aggregate because the longer the light path through the aggregate, the more light can be absorbed (Stemmann & Boss, 2012). Thus, to serve as a useful proxy for porosity (P_{int}), Int needs to be scaled with ESD (in μm) as

$$P_{\text{Int}} = (\text{Int}/255)^2 * \text{ESD} \tag{3}$$

where Int was normalized to its theoretical maximum of 255. Furthermore, we squared Int as its measured range is small compared to the measured range of ESD and would therefore have had only a marginal influence of P_{int} without squaring. The usefulness of P_{int} as an optical proxy for porosity will be discussed in section 4.1.

2.7. Calculation of the RLS

The RLS was calculated by dividing C_{remin} (unit = d^{-1}) by the SV (unit = m/day). Accordingly, RLS can be considered as a *turnover length*, which says how much carbon is respired per meter while POC is sinking to depth. A complicating factor of this calculation was that we had several particle size classes for SV but only the bulk (and not size-dependent) respiration rates. To account for this, we first calculated the individual size dependencies of SV for every mesocosm and day with linear regressions. Second, we used the aggregate size data that were measured on every sampling day with the profiling camera system KIELVISION (see section 2.2). By combining the in situ size of particles measured in each mesocosm on each sampling day with the individual linear regressions calculated in step 1, we calculated the SV for the average size of in situ particles ($SV_{\text{in-situ}}$).

2.8. Estimation of Carbon Transfer Efficiency Through the Mesopelagic

Transfer efficiency (T_{eff}) is defined here as the percentage of sinking POC that makes it from the bottom of the mesocosms (15 m) through the mesopelagic and reaches 1,000 m.

$$T_{\text{eff}} = \left(\frac{\text{POC}_{1000}}{\text{POC}_{15}}\right) * 100 \tag{4}$$

To calculate T_{eff}, we used the following equation derived in Bach et al. (2016):

$$\text{POC}(z) = \text{POC}(z-1) - \left(\text{POC}(z-1)\frac{C_{\text{model}}}{\text{SV}_{\text{model}}}(z-(z-1))\right) \tag{5}$$

where z is the depth (m), C_{model} the model remineralization rate (d^{-1}), and SV_{model} the SV parameterization in the model (m/day). C_{model} decreases with depth due to decreasing temperature (T) following Q_{10} kinetics:

$$C_{\mathrm{model}} = b_{\mathrm{bio}}\, C_{\mathrm{remin}} T^{z} \tag{6}$$

where C_{remin} is the turnover rate measured in this study and b_{bio} is a scaling factor to achieve a realistic flux attenuation (see below for b_{bio} parameterization). For T we used a profile measured near Gran Canaria at the European Station for Time-Series in the Ocean (29.17°N; −15.50°W; Figure S3) on 26 February 2014 during a cruise with R/V *Poseidon* (P465). SV_{model} increases with depth according to

$$SV_{\mathrm{model}} = 0.04z + SV_{\mathrm{in-situ}} \tag{7}$$

The equations for C_{model} and SV_{model} were taken from Schmittner et al. (2008), and their application was justified in Bach et al. (2016). With the average C_{remin} (0.054 day) and $SV_{\mathrm{in\text{-}situ}}$ (37.5 m/day) measured herein (see results) we calculate a mean transfer efficiency from 100 to 1,000 m of 13% with the standard b_{bio} value of 1.066 used earlier (Bach et al., 2016; Schmittner et al., 2008). This flux attenuation is similar to a widely used *Martin b* value of 0.86 (Martin et al., 1987; please note that we used transfer efficiency 100 to 1,000 m [and not 15 to 1,000 m]) in this case to more easily compare the outcome to those by Martin et al. (1987). However, attenuation varies seasonally and regionally (Berelson, 2001) and previous studies reported higher or lower *b* values for the subtropics than 0.86 (Henson, Sanders, et al., 2012; Marsay et al., 2015; Weber et al., 2016). A comprehensive analysis of regionalized flux attenuations calculated 897 *b* values from underwater camera imaging and 1,971 *b* values from POC flux data and found that the median *b* value in the subtropical NE Atlantic to be ~0.6 (Guidi et al., 2015). Thus, we decreased b_{bio} in equation (6) from 1.066 to 1.038 to achieve a mean transfer efficiency from 100 to 1,000 m of 25%, which is equivalent to a *Martin b* value of 0.6 (Guidi et al., 2015; Henson, Sanders, et al., 2012).

The POC mass flux to 1,000 m (POC_{1000}) was calculated as

$$POC_{1000} = POC_{15}\, \frac{T_{\mathrm{eff}}}{100} \tag{8}$$

where POC_{15} is the measured POC mass flux at the bottom of the 15-m deep mesocosms.

3. Results

3.1. Developments in the Plankton Community

The experiment started in oligotrophic conditions with concentrations of all inorganic nutrients close to detection limits (Figure 2). Chl-*a*, POC, and BSi concentrations were low during this period and averaged at approximately 0.1 μg/L, 9 μmol/L, and 0.09 μmol/L, respectively (Figure 2). Deep water was added to all mesocosms on day 24, which increased inorganic nutrient concentrations to 3.15, 0.17, and 1.60 mol/L for NO_x^{-}, PO_4^{3-}, and $Si\,(OH)_4$, respectively. This stimulated a phytoplankton bloom with peak chl-*a* concentrations of 2.61 μg/L on day 28. POC increased correspondingly with a slight delay of about 1–2 days (Figure 2). POC concentrations remained at an elevated level after the bloom and decreased only slowly, while chl-*a* decreased within a few days after the peak. The decline of BSi after the bloom occurred at a rate ranging between those of chl-*a* and POC (Figure 2). TEP concentrations were quite stable and on average 120 μg GXeq L^{-1} before the deep water addition but increased rapidly thereafter right at the point where chl-*a* peaked and nutrients were almost exhausted. TEP declined after peak concentrations but remained at elevated levels until the end of the experiment. The maximum TEP buildup varied considerably between mesocosms, ranging from ~300 (M1) to almost 1100 (M9) μg GXeq L^{-1}.

The phytoplankton community was dominated by picophytoplankton and nanophytoplankton during oligotrophic conditions (days −3 to 24; Figure 3). A bloom of *Synechococcus* (0.6–2 μm) developed during this phase, which peaked around day 11 (Figure 3b). *Synechococcus* abundances declined toward the end of Phase I, while picoeukaryotes (0.2–2 μm) became more important (Figure 3a). Nanophytoplankton made a stable and significant contribution to chl-*a*, while microphytoplankton contributed very little (Figures 3c–3e). The nanophytoplankton contribution remained comparatively stable even after the deep water addition, whereas the relative contribution of picophytoplankton and microphytoplankton reversed. Microphytoplankton was mostly represented by large chain-forming diatoms (*Leptocylindrus* sp., *Guinardia* sp., and *Bacteriastrum* sp.) and the prymnesiophyte *Phaeocystis* sp. (Taucher et al., 2018).
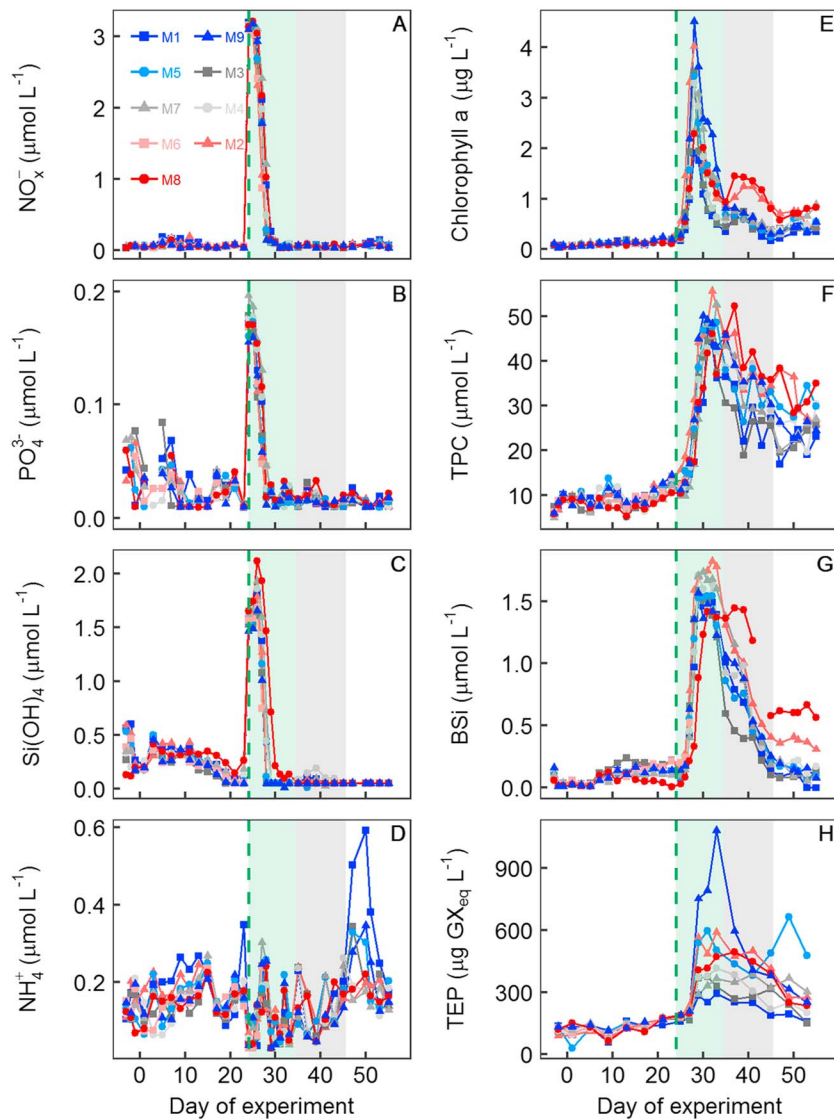
Figure 2. Development of relevant biogeochemical parameters during the experiment. (a) $NO_3^- + NO_2^-$, (b) PO_4^{3-}, (c) $Si(OH)_4$, (d) NH_4^+, (e) chlorophyll a, (f) total particulate carbon, (g) biogenic silica, and (h) transparent exopolymer particles. The green dashed line marks the day of the deep water addition. The green-shaded and the gray-shaded backgrounds denote the time of the phytoplankton bloom and the diatom mass flux event, respectively.

Exceptional to this general pattern were mesocosms M2 and M8 where the toxic phytoplankton species *Vicicitus globosus* (Dictyochophyceae; Chang et al., 2012) contributed majorly to the deep water-induced phytoplankton blooms (Riebesell et al., 2018; Figure 3f).

The zooplankton community comprised protists and metazoa. Protists (i.e., microzooplankton, Figure 4a) were mainly represented by aloricate ciliates and small-sized dinoflagellates (<25 µm). Planktonic foraminifera were an abundant calcifying protist group with all individuals belonging to the family Globigerinidae (Lischka et al., 2018). The most abundant metazoa were copepods, represented primarily by the genera *Paracalanus*, *Clausocalanus*, *Oithona*, and *Oncaea*. Gelatinous zooplankton comprised Hydrozoa with unresolved taxonomic affiliation and tunicates, represented by *Oikopleura dioica* and *Doliolum* sp. A detailed analysis of the zooplankton community can be found in the papers by Lischka et al. (2018), Taucher, Stange, et al. (2018), and Algueró-Muñiz et al. (2019).

Zooplankton abundances were lower during oligotrophic conditions than after the deep water addition except for foraminifera (Figure 4). Most groups responded to the deep water addition with significant
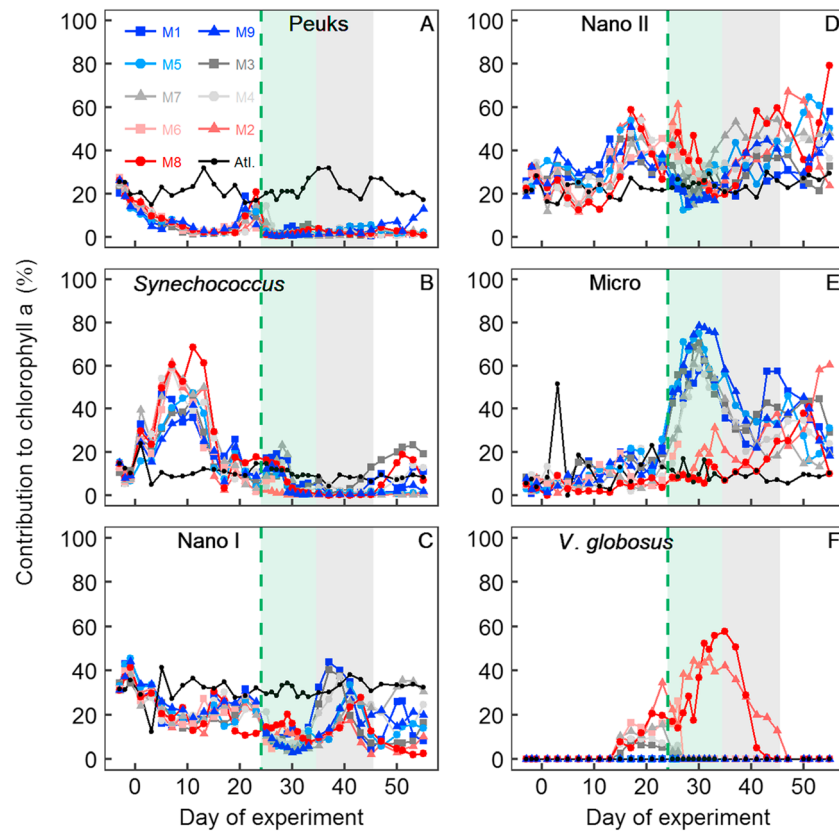
Figure 3. Phytoplankton groups distinguished by means of flow cytometry. Shown here is the contribution of each group to the total concentration of chlorophyll *a* in the water column. (a) Picoeukaryotes (0.2–2 μm), (b) picocyanobacteria (most likely *Synechococcus* spp.; 0.6–2 μm), (c) smaller nanophytoplankton (2–5 μm), (d) larger nanophytoplankton (5–8 μm), (e) microphytoplankton (≫8 μm), and (f) the toxic phytoplankton *Vicicitus globosus* (~20–30 μm). Please note that size range given here accounts for the majority of the gated population but some particles will always be larger or smaller. The plots also show data measured in the Atlantic (black dots) directly next to the mesocosms to illustrate how the enclosure destabilizes the phytoplankton community (section 4.4). The green dashed line marks the day of the deep water addition. The green-shaded and the gray-shaded backgrounds denote the time of the phytoplankton bloom and the diatom mass flux event, respectively.

population growth although the response varied profoundly among mesocosms. For example, microzooplankton and copepods (including nauplii) did not respond positively to the deep water addition in M2 and M8 until the bloom of the toxic phytoplankton *V. globosus* vanished (compare Figures 3f and 4a–4c). The reason for the large variability of microzooplankton and copepod abundances among the remaining mesocosms is unclear at present. Other important differences were the significant blooms of tunicates (*Doliolum* sp.) and hydrozoa in M1. Neither of them grew to high abundances in any other mesocosm, although they were present in all of them (Figures 4e and 4f).

3.2. Mass Flux to the Mesocosm Sediment Traps

The mass flux of biogenic material (G_{cor}) can be separated into three phases. The first one comprises the oligotrophic conditions and the first 10 days after the deep water addition when phytoplankton formed a bloom but the generated biomass was not yet sinking out (days −3 to 34.5). During this initial period, POC, PIC, and BSi mass fluxes averaged at 2.93, 0.32, and 0.14 mmol/m^2 per 48 hr. The second phase lasted for 11 days starting 10 days after the deep water addition when the major diatom (or *V. globosus* in M2 and M8) bloom was sinking out (days 34.5–45.5). POC, PIC, and BSi mass fluxes averaged at 29.7, 0.84, and 2.06 mmol/m^2 per 48 hr during this major sedimentation event. The third phase at the end of the study includes the time after the sedimentation event (days 45.5–55). POC, PIC, and BSi mass fluxes decreased considerably to
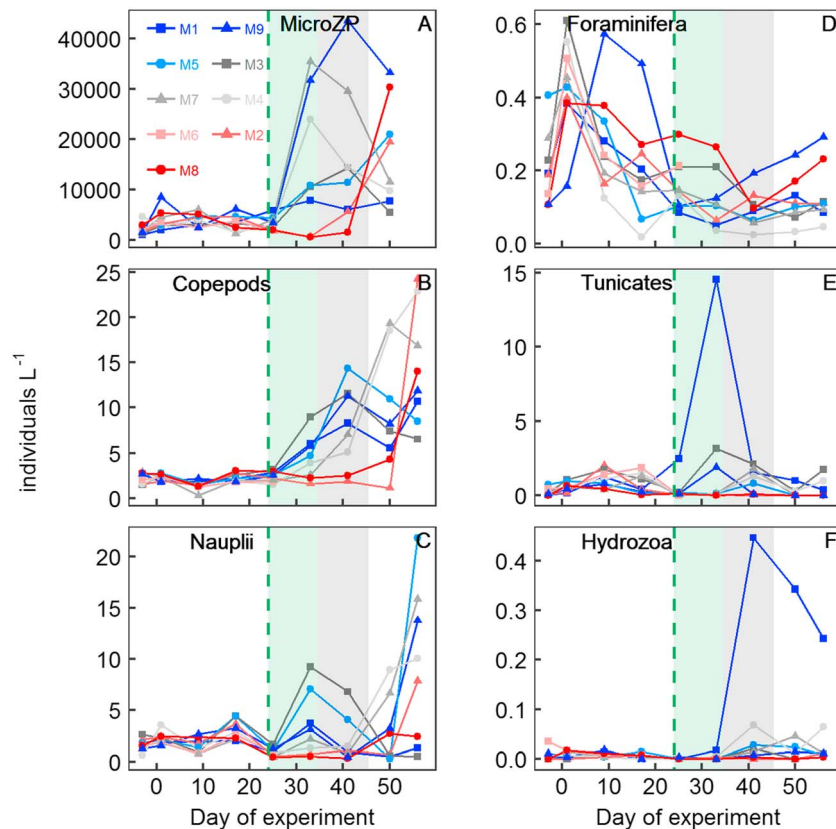
Figure 4. Major zooplankton groups. (a) Microzooplankton, (b) adult copepods and copepodites, (c) nauplii, (d) foraminifera, (e) tunicates, and (f) hydrozoa. The green dashed line marks the day of the deep water addition. The green-shaded and the gray-shaded backgrounds denote the time of the phytoplankton bloom and the diatom mass flux event, respectively.

time-integrated averages of 11.34, 0.29, and 0.42 mmol/m^2 per 48 hr during the three phases, respectively (Figures 5a–5c).

CaCO$_3$ relative to POC export (i.e., PIC:POC) was initially high (~0.4) but decreased exponentially to reach an average ratio of 0.03 after the deep water addition (Figure 5d). Maximum BSi:POC export ratios were considerably lower than PIC:POC and generally more variable (Figure 5e). BSi:POC averaged at 0.075 from days −3 to 1 and dropped to 0.05 thereafter until day 34. BSi:POC increased during the major sedimentation event (average = 0.067), although with quite a large spread among mesocosms (Figure 5e). BSi:POC was lowest after the sedimentation event, averaging at 0.04.

3.3. Particle SV, ESD, P_{int}, C_{remin}, and RLS

We measured SV, ESD, and P_{int} of 62,481 particles during this study. The SVs of the six designated size classes were 26 ± 7.8 (SV$_{40-90}$), 28.2 ± 8 (SV$_{80-130}$), 30.8 ± 10 (SV$_{120-180}$), 35.6 ± 13.4 (SV$_{170-260}$), 43.5 ± 16.8 (SV$_{240-400}$), and 62.2 ± 21.4 m/day (SV$_{380-1000}$), when averaged over all mesocosms and for the entire experiment. The development of SV over time was slightly different among the different size classes but followed a similar overarching pattern (Figures 6a–6f). There was a quite pronounced decline in all size classes after the first measurement day (day 1). Afterward, SV either remained stable (size classes <130 μm) or declined slightly until around day 15. There was a minor peak in SV around day 20 but not in all mesocosms. SV declined from around day 20 until day 45. The decline in this period was particularly pronounced in some size classes during the major bloom sedimentation event (days 34.5–45.5; e.g. 80–130 μm). SV increased thereafter in all size classes (Figures 6a–6f). The temporal development of SV calculated for the average in situ particle size (SV$_{in-situ}$) largely resembled the developments of the largest three size classes (i.e., >170 μm; compare Figures 6d–6f with 7b).
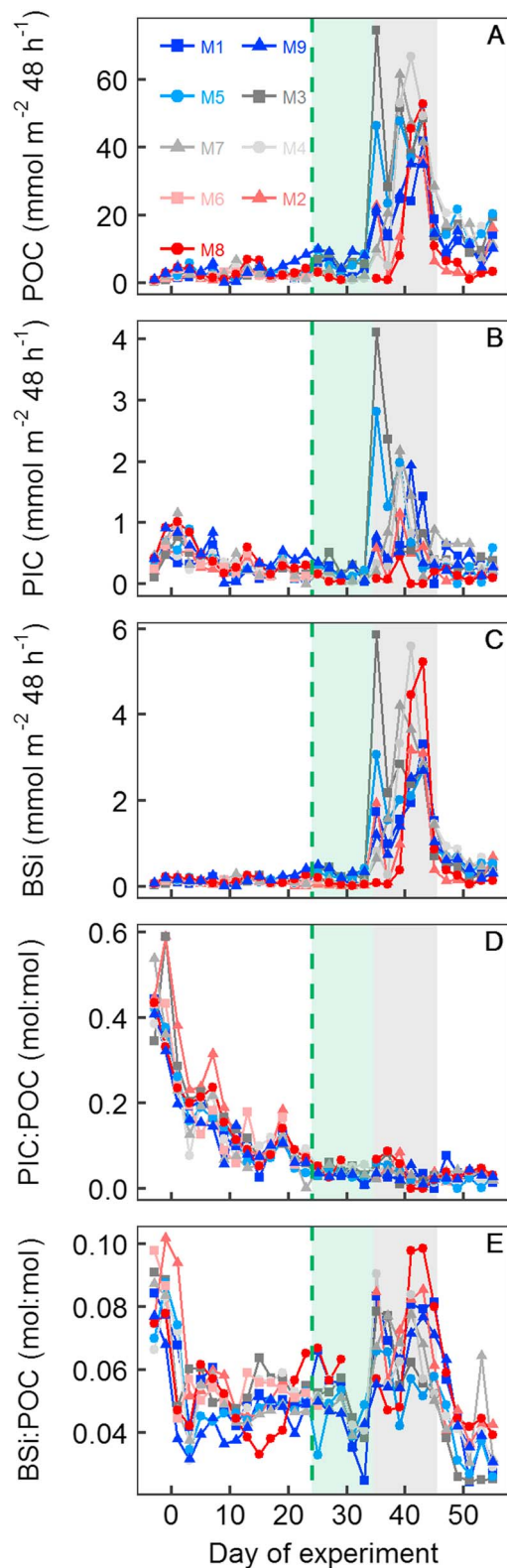
Figure 5. Mass flux of sinking organic material and ballast minerals into the sediment trap. (a) POC, (b) PIC, (c) BSi, (d) PIC:POC, and (e) BSi:POC. The green dashed line marks the day of the deep water addition. The green-shaded and the gray-shaded backgrounds denote the time of the phytoplankton bloom and the diatom mass flux event, respectively.

Mean ESDs of particles within the different size classes were 59 ± 6 (40–90 μm), 101 ± 3 (80–130 μm), 145 ± 4 (120–180 μm), 208 ± 8 (170–260 μm), 305 ± 14 (240–400 μm), and 532 ± 52 μm (380–1,000 μm). The mean values changed only marginally during the experiment (Figures 6g–6l). Thus, changes of mean particle ESD within a size bin cannot explain the pronounced changes in SV of the corresponding size classes. At this point it is important to emphasize that the particle size spectrum determined during the SV measurements is not correctly representing the in situ particle size spectrum. This is because particles used to determine SV have been recovered from the sediment traps through vacuum pumps and have been treated several times before measuring SV in the settling columns (discussed in detail in Bach et al., 2016). To circumvent this problem, we applied a profiling in situ camera system to measure aggregate size spectra in the water column (Taucher, Arístegui, et al., 2018). These measurements revealed that the average size of aggregates between 125 and 3,000 μm was within a range of 200–260 μm for most of the study except for the period of the major sedimentation event where aggregates were larger (Figure 7a). $SV_{in\text{-}situ}$ was affected only to a very small degree by this size increase (Figure 7b).

Mean P_{int} (dimensionless) increased with size: 17.7 ± 1.5 (40–90 μm), 28.1 ± 4.1 (80–130 μm), 37.3 ± 7 (120–180 μm), 48 ± 10.2 (170–260 μm), 64 ± 15.7 (240–400 μm), and 99.6 ± 25 (380–1,000 μm). Accordingly, P_{int} reproduces the expected increase of porosity with size (Burd & Jackson, 2009; Logan & Wilkinson, 1990) due to the dependency of P_{int} on ESD (see equation (3)). P_{int} was increasing in most size classes until the major bloom sedimentation event (Figures 6m–6r). The increase was larger in the smaller size classes, and hardly any change was observed in the two largest size classes. P_{int} increased rapidly at the onset of the sedimentation event. Conversely to the trends prior to this event, the increases were more pronounced in the larger size classes. In this case, no increase was observed in the smallest size class. P_{int} decreased to a variable degree in all size classes after the bloom sedimentation (Figures 6m–6r). SVs of all size classes were negatively correlated with P_{int} (Figure 9a).

POC remineralization (C_{remin}) was determined on nine occasions during the mesocosm experiment (Figure 7c). Unfortunately, technical problems with the equipment prevented us from doing incubations before day 11. The estimated C_{remin} uncertainty of 35% (section 2.4) and the lower temporal resolution of this data set complicated the detection of trends over time since only very clear changes can be distinguished from noise (Figure 7c). On average, C_{remin} was higher during the first incubation with the highest value in M9 (0.125 day), while the lowest C_{remin} was observed in M8 during the phytoplankton bloom (0.007 day). High values were also measured during the major sedimentation event (days 37 and 41), although only in M3, M5, and M7. C_{remin} declined in almost all mesocosms after the sedimentation event (Figure 7c).

RLS ranged between 0.0002 and 0.004 m^{-1}, and the temporal development largely resembled the development of C_{remin} (compare Figures 7c and 7d). The influence of C_{remin} on RLS was dominant because its changes during the study were approximately fifteenfold, while the changes in $SV_{in\text{-}situ}$ were approximately threefold (compare Figures 7b and 7c). Nevertheless, $SV_{in\text{-}situ}$ had a noticeable influence on RLS due to
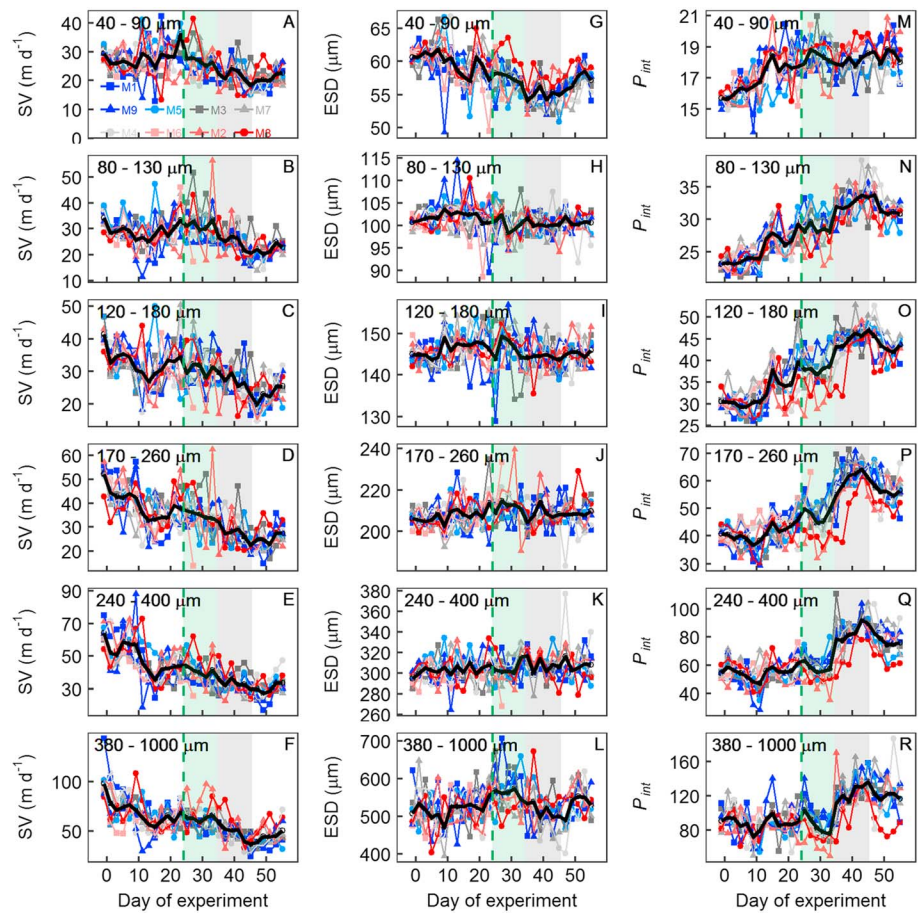
Figure 6. Temporal development of sinking velocity (SV), ESD, and the porosity proxy P_{int}. (a–f) SV of the different particle size classes, (g–l) mean ESD, and (m–r) P_{int} of the corresponding size classes. Please note that the size classes are reported at the top of each subplot. The black line on each plot is the daily average of all mesocosms and is shown to facilitate the detection of general trends. The green dashed line marks the day of the deep water addition. The green-shaded and the gray-shaded backgrounds denote the time of the phytoplankton bloom and the diatom mass flux event, respectively.

the generally decreasing trend from initially ~50 to ~30 m/day at the end of the study. This decrease was reflected in particularly high RLS during the major sedimentation event.

3.4. Estimated Transfer Efficiency and Mass Flux to the Deep Ocean

The degree of flux attenuation varied widely over the course of the study, largely driven by the fluctuations in C_{remin}. Accordingly, the temporal pattern of T_{eff} largely resembled the inverse of C_{remin} (compare Figures 7c and 8b). T_{eff} ranged from 0.6% to 74% with the majority of values between 0.6% to 20%. POC_{1000} ranged between 0.01 and 4.8 mmol/m^2 per 48 hr and was generally higher during the mass flux event than during oligotrophic conditions (Figure 8c).

4. Discussion

4.1. P_{int}—A Useful Optical Proxy for Aggregate Porosity?

Porosity indicates the fraction of an aggregate not occupied by solid matter (Alldredge & Gotschalk, 1988). A porous aggregate will usually have a lower density and therefore sink slower than a more compact one, given that both have the same size, shape, and are made of solid matter of a similar density. Thus, porosity is an important variable affecting aggregate SV and ultimately POC export (Burd & Jackson, 2009).
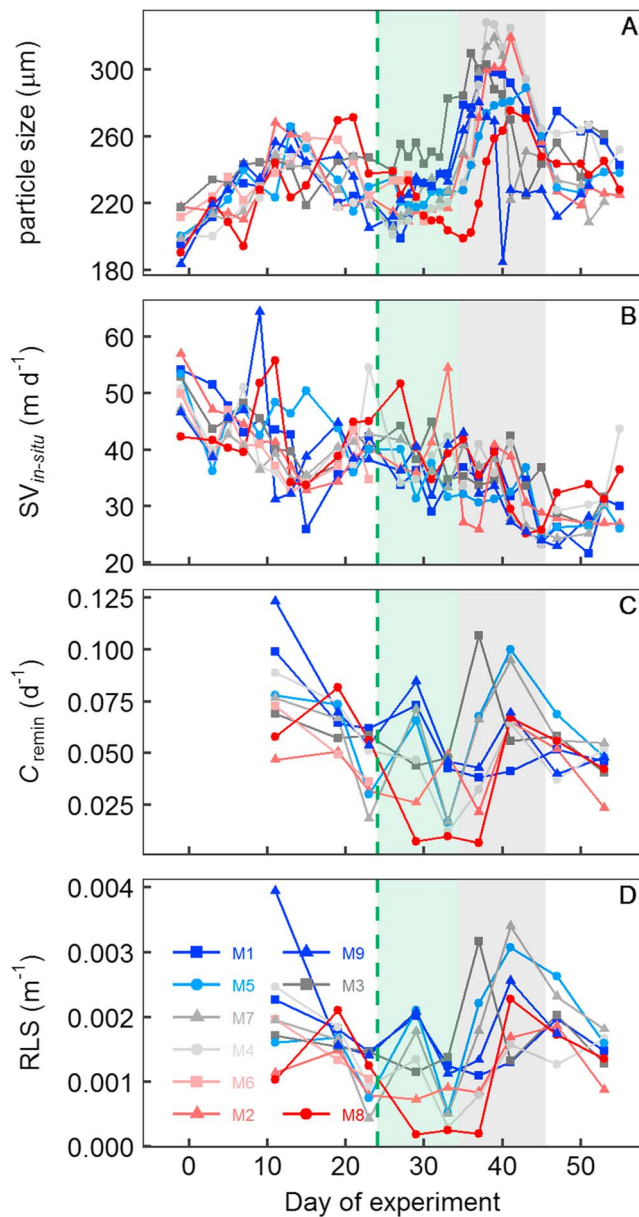
Figure 7. Size, $SV_{in\text{-}situ}$, and remineralization of sinking material. (a) Average size of particles >125 µm inside the mesocosms as determined with an in situ camera system. (b) $SV_{in\text{-}situ}$ calculated with daily ESD versus SV relationships measured with the FlowCam using in situ particle size as input data. (c) C-specific remineralization rate (C_{remin}). (d) Remineralization length scale. The green dashed line marks the day of the deep water addition. The green-shaded and the gray-shaded backgrounds denote the time of the phytoplankton bloom and the diatom mass flux event, respectively.

Porosity can be measured directly by embedding aggregates in resins or gels and thin slicing them to determine their structure microscopically (Chu et al., 2004; Flintrop et al., 2018; Leppard et al., 1996). These measurements provide an unprecedented level of detail of the aggregate matrix but are too time-consuming and expensive to apply to the thousands of aggregates investigated here. Alternatively, porosity can be calculated from dry weight measurements or density estimations, but these calculations are associated with numerous assumptions and must be regarded with care (Alldredge & Gotschalk, 1988; Engel et al., 2009; Logan & Wilkinson, 1990; Helle Ploug et al., 2008). Here we derive *size-normalized particle intensity* (P_{int}) as an independent and easily measurable proxy for porosity. The underlying assumption is that aggregates within a narrow size range appear brighter when they are more porous because more of the light passes through the back-light-illuminated aggregate (section 2.6).

The best way to assess the value P_{int} would be a comparison to an independent porosity approximation. In similar data set from the Norwegian coast, we estimated porosity from calculated aggregate excess densities and solid matter density of sediment trap material using Stokes' law (Bach et al., 2016). Unfortunately, Stokes' law was not applicable in the present experiment because SV (and therefore Reynolds numbers) were too high so that most particles did not sink in a laminar flow regime (McNown & Malaika, 1950). Thus, at this stage we can only argue that P_{int} is a useful proxy without independent validation. Perhaps the strongest support for its usefulness comes from the pictures shown in Figure 1. These were taken randomly from measurements in M3 and show that aggregates with higher P_{int} values on the right side of Figure 1 do indeed appear to be more porous. The porous aggregates were filmed mostly during the mass flux event where concentrations of TEP were considerably higher (Figure 2h). TEP serves as glue within the aggregate matrix, and high concentrations should increase the probability to find loosely attached phytoaggregates, which have not experienced much (re) packaging (Burd & Jackson, 2009). However, P_{int} could also be affected by the chemical composition of the aggregate matrix, which, like porosity, influences the intensity (i.e., the *brightness*) of a particle. For example, interstitial space in aggregates could be filled with $CaCO_3$ or TEP, and this would in both cases reduce the porosity. However, $CaCO_3$ absorbs more light than TEP and therefore affects P_{int} differently. The problem of material transparency could be circumvented to some extent by staining transparent components within the aggregate matrix (Cisternas-Novoa et al., 2015), but this has not been done here. Thus, the unknown chemical composure of aggregates must be considered as confounding factor for the porosity approximation with P_{int}.

The temporal development of P_{int} reveals distinct features that further strengthen our confidence in this proxy. For example, there was a sudden increase of P_{int} at the onset of the mass flux event (see Figures 6m–6r, particularly the larger size classes). We observed exactly the same kind of sudden increase during the onset of mass flux event in a mesocosm study at the Norwegian coast where porosity was assessed differently (Bach et al., 2016). Thus, the similarity in the response patterns with two independent porosity approximations supports both of them.

Furthermore, the mesocosm-specific development of P_{int} during the mass flux event provides additional support. The major bloom formers after the deep water addition were diatoms, but these were less
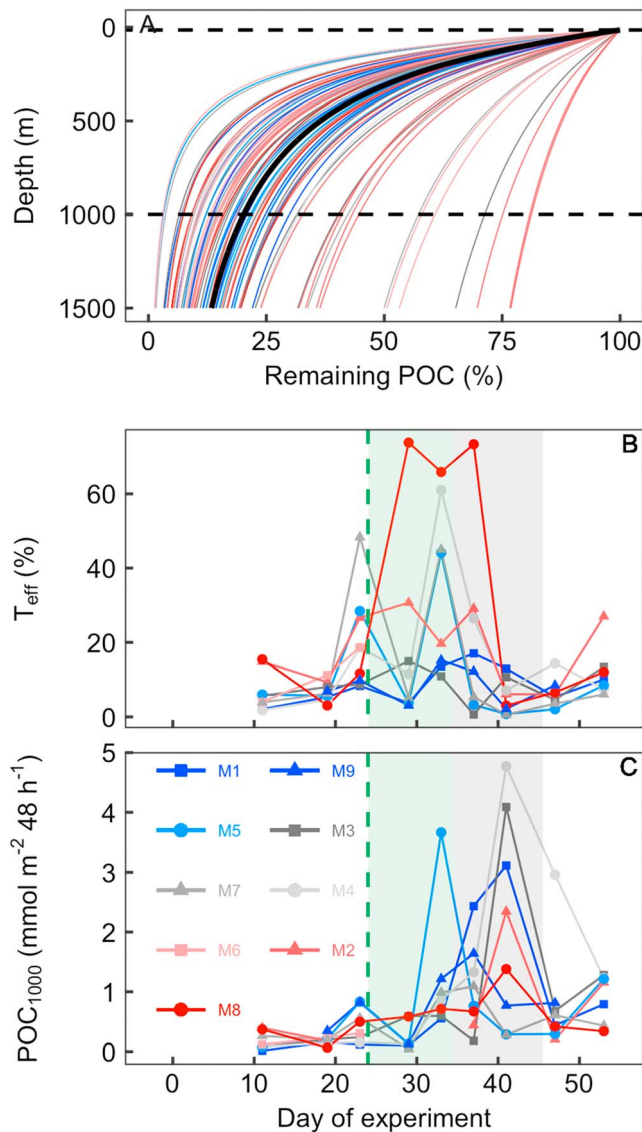
Figure 8. Transfer efficiency (T_{eff}) and mass flux to the deep ocean based on $SV_{in\text{-}situ}$ and C_{remin} using model equations (4) and (5). (a) Calculated flux attenuation profiles of organic material collected in the mesocosm sediment traps while sinking to depth. Each of the 73 thin lines represents one attenuation profile as calculated with equation (5) using one of the 73 measured C_{remin} values and the 73 corresponding $SV_{in\text{-}situ}$ values, respectively (C_{remin} values from Figure 7c and corresponding $SV_{in\text{-}situ}$ from Figure 7b). The color code corresponds to the mesocosms where the $SV_{in\text{-}situ}$ and C_{remin} combination was measured. The thick black line is the attenuation profile calculated with the average of all 73 C_{remin} values (i.e., 0.054 day) and the average of the corresponding 73 $SV_{in\text{-}situ}$ values (37.5 m/day). The horizontal dashed black lines mark the 15- (bottom of mesocosm) and 1,000-m depths, respectively. (b) T_{eff} between 15 and 1,000 m derived from calculations with equation (5). These are the intercepts where the individual profiles from plot (a) cross the 1,000-m depth level. (c) Mass flux at 1,000-m depth as calculated with equation (8). The green-shaded and the gray-shaded backgrounds in (b) and (c) denote the time of the phytoplankton bloom and the diatom mass flux event, respectively.

abundant in M8 than in the other mesocosms at the day of deep water addition (Figure 2g). Accordingly, the diatom bloom was delayed by 2–4 days in M8 relative to the other mesocosms as is reflected in all Si data sets (Figures 2c, 2g, and 5g). Interestingly, this delay in diatom bloom formation is also reflected in P_{int} for particles >120 μm (Figures 6o–6r) and in the in situ particle size data set recorded with the underwater camera system (Figures 7a). The most plausible explanation for such a consistency in three entirely independent measurements is that P_{int} increases due to the formation of highly porous diatom aggregates, combined with the lack of microzooplankton and mesozooplankton grazers during this period (check Figure 4 for zooplankton). This adds additional confidence to the value of P_{int} as porosity proxy.

Vertical particle profiles determined with in situ camera systems are becoming an increasingly important tool to estimate carbon export fluxes (Boss et al., 2015; Guidi et al., 2008; Iversen et al., 2010). Camera-based mass flux calculations utilize particle abundance data and a theoretical size versus SV relationship (Guidi et al., 2008). However, Figure 6 illustrates that size alone is insufficient to predict SV as it changes approximately threefold in the course of the study, while aggregate sizes remain largely constant. The utilization of the P_{int} versus SV relationships shown in Figure 9a may therefore help to improve the determination of mass flux, at least with back-light-illuminated camera systems where P_{int} could be determined.

4.2. Influence of Ballast Minerals and Plankton Community Structure on SV

The development of SV over time reveals distinct patterns that can be linked to processes in the plankton community. SV was relatively high during the first 2 weeks of the experiment, particularly in the size classes >170 μm (Figures 6a–6f). One likely reason for this was the initially high ballasting with $CaCO_3$ (Figure 5d), but the question is what generated this ballast? The two calcifying groups that were found in relevant quantities were coccolithophores and foraminifera (Lischka et al., 2018; W. Guan, personal communication). Coccolithophores were present only until the deep water addition in abundances fluctuating between below detection limit and 1.5 cells per milliliter (W. Guan, personal communication). If we assume a per cell PIC content of a heavily calcified species (25 pmol per cell for *Coccolithus pelagicus*; Bach et al., 2015), we would in the highest possible case (1.5 cells per milliliter) reach a coccolithophore PIC of 0.04 μmol/L. Hence, if such an amount sank out in 48 hr (i.e., 0.43 mmol/m^2 per 48 hr), it could explain the initial PIC flux to the sediment traps (Figure 5b). However, since the 0.04 mmol/L is an upper bound, we consider coccolithophores to contribute generally much less $CaCO_3$ ballast. Foraminifera were represented by very small (50–200 μm) Globigerinidae species (Lischka et al., 2018). The highest measured sedimentation flux was 0.14 individual per liter per 48 hr (~1,500 individuals per square meter per 48 hr) but generally well below this value (Lischka et al., 2018). Based on published size to weight relationship for the two Globigerinidae species (Lombard et al., 2010), we estimate that a 200-μm individual would have contained less than 10-μg $CaCO_3$ (~0.1-μmol PIC). Thus, the PIC flux by foraminifera tests could maximally have been 0.15 mmol/m^2 per 48 hr, but likely much lower most of the time. Furthermore, foraminifera shells do not integrate particularly well into aggregate matrices so that their accelerating effect on SV should be minor (Schmidt et al., 2014).
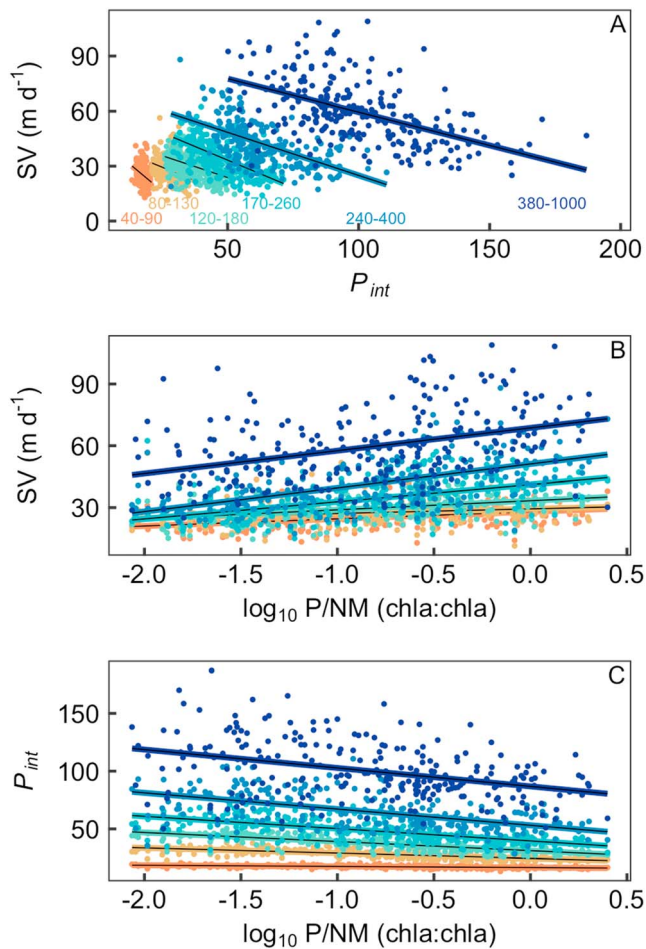
Figure 9. Correlations between SV, P_{int}, and the ratio of picophytoplankton to nanophytoplankton and microphytoplankton (P/NM). The different colors from warm to cold represent the six different particle size classes: orange = 40–90 μm, yellow = 80–130 μm, turquoise = 120–180 μm, blue-green = 170–260 μm, blue = 240–400 μm, and dark blue = 380–1,000 μm (see also the legend in the top panel). All correlations shown here are significant ($p \ll 0.01$). (a) SV is negatively correlated with P_{int} in all size classes; $R^2_{40-90} = 0.09$, $R^2_{80-130} = 0.12$, $R^2_{120-180} = 0.21$, $R^2_{170-260} = 0.38$, $R^2_{240-400} = 0.34$, $R^2_{380-1000} = 0.27$. (b) SV is positively correlated with P/NM in all size classes; $R^2_{40-90} = 0.14$, $R^2_{80-130} = 0.04$, $R^2_{120-180} = 0.14$, $R^2_{170-260} = 0.27$, $R^2_{240-400} = 0.31$, $R^2_{380-1000} = 0.15$. (c) P_{int} is negatively correlated with P/NM in all size classes; $R^2_{40-90} = 0.18$, $R^2_{80-130} = 0.47$, $R^2_{120-180} = 0.49$, $R^2_{170-260} = 0.41$, $R^2_{240-400} = 0.30$, $R^2_{380-1000} = 0.14$. Please note that the x axis scaling in b and c is log10 transformed and the numbers on the axis show the exponent (e.g., $-1 = 10^{-1} = 0.1$ chla:chla). Regression equations are provided in Table S1.

Based on the above mentioned assessments, it seems unlikely that biogenic $CaCO_3$ is fully accountable for the PIC mass flux observed in the mesocosm sediment traps. Lithogenic carbonates could enter the mesocosms at the surface via airborne dust influx, which regularly occurs in the Canary Island region (Gelado-Caballero et al., 2012; Neuer et al., 2004; Nowald et al., 2015), although dust dry deposition was not particularly high during the first week of the study when PIC:POC was highest (D. Gelado-Caballero, personal communication). Alternatively, resuspended carbonate sediments enclosed initially may have started to sink out as soon as the mesocosms were closed and the turbulence declined. The exponentially decreasing PIC:POC ratio in the sediment traps lends some support for this hypothesis (Figure 5d).

The plankton size structure was likely another important reason for generally higher SV during the first half of the study. P_{int}, our proxy for porosity, was generally lower during the first 2 weeks indicating that the plankton community produced relatively compact detritus when oligotrophic conditions prevailed (Figures 1 and 6m–6r). Oligotrophy is usually characterized by the dominance of picophytoplankton and small nanophytoplankton (Chisholm, 1992), which provide small aggregate building blocks allowing little interstitial space between them when they aggregate (Burd & Jackson, 2009). Furthermore, organic biomass is considered to be recirculated more intensely through the food web under stable oligotrophic conditions thereby generating higher aggregate compactness than in more unstable environments (Fischer & Karakaş, 2009; Francois et al., 2002; Lam et al., 2011). However, we consider this second mechanism not to be relevant in our study because the enclosure of the phytoplankton communities destabilized the oligotrophic food web as will be argued in section 4.5.

The deep water addition on day 24 initiated a phytoplankton bloom, which quickly ran into nitrogen limitation and peaked around day 29 (Figures 2a, 2e, and 2g; Taucher, Stange, et al., 2018). TEP concentrations increased sharply after the chl-a peak and promoted the initiation of an aggregation event that lasted for 10 days until aggregates reached their maximum size and sank down during the mass flux event between days 35 and 48 (Figures 2h and 5a; Stange et al., 2017; Taucher, Arístegui, et al., 2018). The diatom bloom and the simultaneous formation of increasingly large aggregates coincided with a considerable reduction of SV, even though opal ballast increased during the mass flux event (Figures 6a–6f and 5e). Thus, the accelerating influence of opal ballast on aggregate excess density must have been overcompensated by reduced compactness. There are four lines of evidence supporting this conclusion. First, nutrient injections into the prevailing oligotrophic conditions shifted the phytoplankton size structure toward larger species (Figure 3). Larger species should form more porous aggregates because (i) they provide more interstitial space within the aggregate matrix and (ii) they are transiently relieved from biotic repackaging because they outgrew copepod grazers (compare Figures 2e and 4b). Indeed, P_{int} increases substantially during the mass flux event which is not only very clear in the data (Figures 6m–6r but with the exception of 40–90 μm) but also obvious when comparing pictures of aggregates from the mass flux event with those photographed during the oligotrophic phase (Figure 1). Second, relatively high concentrations of TEP after the bloom (Figure 2h) may have decelerated sinking because TEP is positively buoyant and, due to its stickiness, causes a more porous aggregate structure, which further reduces their excess density (Azetsu-Scott & Passow, 2004; Engel & Schartau, 1999; Mari, 2008; Mari et al., 2017). Third, we have made the identical observation during diatom blooms in the mesocosm study in Norway and came to the same porosity-based

Table 1
C-Specific Remineralization (C_{remin}) Measurements From the Literature

Reference	Aggregate	Depth (m)	Collection	Method	RQ	T (°C)	C_{remin} (d^{-1})	Aggregate origin
Belcher et al. (2016)	FP	0–200	Net haul	O_2 diffusion	1	3-5	0.010–0.065	Southern Ocean
Cavan and Boyd (2018))	Detritus	30	Mesh	O_2 decline	1	12	0.97 ± 0.10[a]	Southern Ocean
Cavan et al. (2017)	Detritus	50–350	MSC	O_2 decline	1	24	0.35–13.7[b]	Equatorial Pacific
Collins et al. (2015)	Detritus	50–300	Trap	O_2 decline	1.45	in situ	0.007–0.173	North Atlantic
Goldthwait et al. (2005)	Detritus	13–20	Diver	POC decline		18	0.1–0.63	NE Pacific
Iversen et al. (2010)	RT[c]			O_2 diffusion	1.2	18–20.4	0.13 ± 0.07	NE Atlantic
Iversen and Ploug (2010)	RT			O_2 diffusion	1.2	15	0.13 ± 0.13	
Iversen and Ploug (2013)	RT			O_2 diffusion	1	12	0.12 ± 0.03	
Iversen and Ploug (2013)	RT			O_2 diffusion	1	4	0.03 ± 0.01	
Iversen et al. (2017)	FP[d]		Salp	O_2 diffusion	1.2	3	0.05 ± 0.5	Southern Ocean
Le Moigne et al. (2013)[e]	RT			POC decline		15	0.03–0.05	
Le Moigne et al. (2017)[e]	Detritus	40–180	Trap	POC decline		12	0.002–0.05	Baltic Sea
Mcdonnell et al. (2015)	Detritus	200–500	Trap	RESPIRE	1.45	in situ	0.4 ± 0.1	Sargasso Sea
Mcdonnell et al. (2015)	Detritus	50	Trap	RESPIRE	1.45	in situ	0.01 ± 0.02	Southern Ocean
Ploug and Bergkvist (2015)	RT			O_2 diffusion	1	10	0.065[f]	
Ploug and Grossart (2000)	RT			O_2 diffusion	1	16	0.2–0.03	
Ploug et al. (1999)	Detritus	0–15	Diver	O_2 diffusion	1.2	17	0.11–0.13	NE Pacific
This study	Detritus	15	Trap	O_2 decline	1	22	0.007–0.1	NE Atlantic

Note. Aggregate describes whether detritus or fecal pellets (FP) were collected or whether aggregates were produced using roller tanks (RT). *Depth* indicates where in the water column they were collected. *Collection* describes how they were collected (Net haul = collected with vertical net hauls or trawls; Mesh = pumped onto a 200-μm mesh; MSC = Marine Snow Catcher; Trap = collected with sediment traps; Diver = collected in situ by divers; Salp = fecal pellets formed in vitro by salps). *Method* indicates how respiration was measured: (1) O_2 diffusion in flow chamber, (2) assay incubation measuring O_2 decline, (3) change of aggregate POC over time, and (4) in situ incubations with REspiration of Sinking Particles In the subsuRface ocean RESPIRE sediment traps (Boyd et al., 2015). *RQ* is the applied respiratory quotient (mol O_2: mol CO_2). *T* is the incubation temperature of the respiration measurements. [a]Up to 5.25 days for future ocean temperature simulations. [b]0.13–5 days when correcting for offset between incubation and in situ temperature; high values only in small/slow sinking particles. [c]Natural source water and aggregates generated with roller tanks. [d]Natural source water was offered to salps collected on site who then generated fecal pellets in vitro. [e]Values recalculated from the original data set be F. Le Moigne to C-specific remineralization in d^{-1} (F. Le Moigne personal communication, 2019) [f]Hypoxic conditions.

conclusion for the reduction in SV even though porosity was estimated in a different manner (Bach et al., 2016). Fourth, several field studies reported that mass fluxes of coagulated diatom aggregates are associated with relatively high flux attenuation, which points toward decelerated sinking despite high ballast availability (Fischer & Karakaş, 2009; Francois et al., 2002; Guidi et al., 2009; Henson, Lampitt, et al., 2012; Kiørboe et al., 1998; Lam et al., 2011; Lam & Bishop, 2007; Lutz et al., 2007; Maiti et al., 2013; Puigcorbé et al., 2015). Hence, in line with earlier studies, we conclude that the high porosity of TEP-rich diatom aggregates reduces SV.

To further explore the influence of the phytoplankton size structure on sinking, we computed the biomass ratio of picophytoplankton to nanophytoplankton and microphytoplankton (P/NM) as an *ecosystem indicator* using the fluorescence data shown in Figure 3. The idea is that a high P/NM prevails under oligo- trophic conditions where small primary producers enable the formation of compact particles (see above). Nutrient injections provide resources for larger phytoplankton to grow thereby driving the close coupling between small autotrophs and associated heterotrophs out of equilibrium. Hence, in a low P/NM regime, porous aggregates may enter the export pathway before significant repackaging by heterotrophs has occurred. Indeed, P/NM has previously been useful to predict export flux attenuation (Guidi et al., 2009, 2015) and SV (Bach et al., 2016). As in Bach et al. (2016), we find significant positive correlations between SV and P/NM (Figure 9b). Furthermore, we provide independent evidence for a key mechanism driving this correlation—that is, the decrease of aggregate porosity with an increasing dominance of picophytoplankton (Figure 9c). P/NM is readily measured by flow cytometry (section 2.2), can be estimated for the surface ocean with satellite data (Mouw et al., 2017), and is accessible in biogeochemical models with size-structured food webs (Ward et al., 2012). Thus, accounting for the dependency of SV on P/NM could improve our ability to estimate export fluxes with optical tools and in biogeochemical models (Guidi et al., 2015; Siegel et al., 2014). Ultimately, this may be a significant step toward a better predictability of BCP strength and efficiency in a future ocean where picophytoplankton could become more dominant (Bach et al., 2017; Boyd, 2015).

4.3. Comparison of Carbon-Specific Remineralization (C_{remin}) With Values Reported in the Literature

C_{remin} determined here is within the range of previously reported values but on the lower end of the spectrum (Table 1). The relatively low values are somewhat surprising as our incubation temperature (T) of 22 °C was high compared to other studies (Table 1). For instance, C_{remin} was at least an order of magnitude higher for particles collected at the Southern Ocean Time Series, even though T was 10 °C lower (Table 1; Cavan & Boyd, 2018). Likewise, our values were at least 4 times lower than C_{remin} measured in situ at the Bermuda Atlantic Time-series Study (Table 1; Mcdonnell et al., 2015) even though the oceanographic setup is relatively similar.

The exact reasons for observed differences are difficult to determine as there is no obvious pattern in relation to T or location (Table 1). Clearly, the biodegradability of POC will vary widely between particles. Thus, a large spread is not necessarily unexpected. Also, a variable degree of DOC leakage from sinking POC may create uncertainty because DOC leakage is typically not quantified (but see Goldthwait et al., 2005). Furthermore, methodological differences will play an important role. C_{remin} has been determined using different approaches, all of which involve assumptions and measurements with considerable uncertainties (Table 1). The RQ, for example, is a large source of uncertainty. It is typically assumed to be constant and somewhere between 1 and 1.5 (Table 1), but deviations of ± 0.2 or more are frequently observed due to changes in POC quality and community characteristics (Berggren et al., 2012; Robinson & Williams, 1999). In our approach we assumed an RQ uncertainty of $\pm 20\%$, which could perhaps be eliminated in future studies by using CO_2 instead of O_2 optode measurements.

Interestingly, measured C_{remin} seems to converge to a narrower range when similar protocols were applied. Our C_{remin} values compared well with the range reported by Collins et al. (2015) who used O_2 consumption bioassays in an almost identical setup. C_{remin} reported by Cavan et al. are generally on the higher end of the spectrum (Table 1). C_{remin} determined with the diffusion method often yields values around 0.1 day unless assays are performed with fecal pellets, in very cold water, or hypoxic conditions where C_{remin} tends to be lower (Table 1). Thus, while the natural variance of C_{remin} is certainly high, some of the spread may also be due to different methodology and assumptions (e.g., different RQ). It may therefore be worthwhile to intercompare methods and establish common protocols since C_{remin} is a parameter of highest biogeochemical relevance.

4.4. Influence of Plankton Community Structure on C_{remin}, RLS, T_{eff}, and Estimated Deep Ocean Carbon Flux

Our simultaneous measurements of C_{remin} and SV showed that C_{remin} is much more sensitive to changes in the plankton communities than SV. The maximum difference in C_{remin} was approximately fifteenfold, while SV changed merely approximately threefold (compare Figures 7b and 7c). Thus, the plankton community controls RLS and also T_{eff} primarily by influencing C_{remin}.

Unfortunately, determining C_{remin} is relatively labor-intensive leading to a lower temporal resolution than what is available for the SV data set. Additionally, we estimated a comparatively high uncertainty of $\sim \pm 35\%$, which further complicated the detection of trends over time. Thus, only particularly pronounced changes were sufficiently clear and consistent to distinguish them from noise and link them to processes in the plankton community.

C_{remin} was high during days 11 and 19 leading to high RLS and low T_{eff} (Figures 7c, 7d, and 8b). These results suggest that the BCP is rather inefficient under oligotrophic conditions, which disagrees with findings from numerous previous studies (Buesseler & Boyd, 2009; Guidi et al., 2009, 2015; Henson, Sanders, et al., 2012; Lam et al., 2011; Mouw et al., 2016; but see also Marsay et al., 2015; Weber et al., 2016). However, we argue that our measurements are influenced by mesocosm-specific developments in the plankton communities, which differ from the *typical* oligotrophic regime. Oligotrophic conditions outside the mesocosms are characterized by relatively stable phytoplankton communities (Figure 3), suggesting a close coupling between autotrophs and heterotrophs where significant blooms do not occur. The enclosure inside the mesocosms clearly destabilized the oligotrophic community and gave room for fluctuating bloom developments as seen in all phytoplankton groups (Figure 3). The phytoplankton size structure remained dominated by smaller

groups (Figure 3), which conserve relatively low P_{int} and high SV (Figure 6) probably by providing small aggregate building blocks (section 4.2). Yet, fluctuating conditions likely reduce the recycling of biomass through the food web and allow a higher fraction of fresh and less degraded material to sink out (Giering et al., 2017; Henson et al., 2015). The C:N ratio of the sinking material supports this hypothesis as it was lowest during days 11–19 (10.8 ± 1.1 versus 13.3 ± 2.1 between days 21 and 53; Stange et al., 2018). In contrast, the field-based evidence that led to a prevailing view of high BCP efficiency under oligotrophic conditions (Sarmiento & Gruber, 2006) argues on the basis of stable conditions where biomass recycling within the food web should be more intense. Thus, C_{remin}, RLS, and T_{eff} determined during days 11 and 19 may not be representative for the *stable* oligotrophic regime with a close coupling between autotrophs and heterotrophs but for one that is *out of equilibrium*.

C_{remin} and RLS were lowest during days 29 to 37 in M8 and to a lesser extent in M2 (Figures 7c and 7d). This period coincided with the bloom of the toxic algae *V. globosus*, which disrupted trophic transfer by inhibiting zooplankton growth (Figures 3f and 4; Riebesell et al., 2018). The toxicity of *V. globosus* has very likely reduced POC degradation by bacteria and/or zooplankton where the latter were considerably less abundant in M8 and M2 (Figure 4; Riebesell et al., 2018). Importantly, the harmful algal bloom (HAB) co-occurred with a pronounced diatom bloom in M2, while the diatom bloom was much weaker and delayed relative to the HAB in M8 (Taucher, Stange, et al., 2018). Thus, the sinking material in M2 contained a higher fraction of *nontoxic* detritus, which explains why C_{remin} and RLS were relatively higher in M2 than in M8 during the HAB (Figure 7c). The lowest RLS values in M8 lead to the highest modeled T_{eff} values (equations (4) and (5)) during the experiment with ~74% of the sinking material reaching 1,000 m (Figure 8b). This suggests that HABs are particularly efficient in injecting carbon into the deep ocean. However, the mass flux to 1,000 m was still relatively small since the export production at 15 m was low during the HAB (Figure 8c).

RLS and C_{remin} had temporal maxima (and T_{eff} temporal minima) during the mass flux event albeit at different days and in some mesocosms much more pronounced than in others (Figures 7c, 7d, and 8b). We attribute the decreasing T_{eff} during this period to the enhanced availability of fresh and TEP-rich aggregates, which formed during the bloom (Taucher, Stange, et al., 2018). These should be more easily degradable because the turnover of TEP is about twice as high as the turnover of the associated cellular POC (Mari et al., 2017). However, it is important to note that relatively high TEP concentrations also led to 35% increased C:N ratios of the sinking material (POC:PON $\approx$ 10 on days -3 to 29 versus $\approx$13.6 on days 31–55; Stange et al., 2018), which counteracts the reduction of T_{eff} by the same percentage because sinking POC carries more carbon. POC_{1000}, and thus *the strength of the BCP*, increased during the mass flux event because the massive increase in export production overcompensated the reduction in T_{eff}. This agrees well with repeated observations of high mass flux at relatively low T_{eff} during diatom blooms (e.g., Fischer & Karakaş, 2009; Henson, Sanders, et al., 2012; Lam et al., 2011).

5. Summary and Outlook

In this study we used in situ mesocosms to investigate the influence of a subtropical plankton community structure on POC SV and C-specific remineralization rates (C_{remin}). In accordance with earlier studies, we find that SV is accelerated by $CaCO_3$ ballast, while the influence of BSi ballast was less obvious. This could either be due to the relatively low concentrations of BSi relative to POC and/or because the positive BSi ballast effect on aggregate density was overcompensated by a negative effect of increased aggregate porosity which co-occurred during the diatom bloom after the deep water addition.

We propose P_{int} as potentially useful optical proxy for porosity and find that aggregates have on average a lower P_{int} (i.e., they are less porous) when the phytoplankton community is dominated by smaller species, which form smaller aggregate building blocks. Thus, our results provide new evidence for previous findings that the phytoplankton size structure can serve as a useful proxy to estimate export efficiency (Guidi et al., 2009) and for the first time provide data that allow us to mechanistically link this observation directly to porosity.

The key finding of our study is that plankton community structure seems to have a considerably larger influence on C_{remin} than on SV. C_{remin} tended to be higher when relatively fresh material from an ongoing/decaying phytoplankton bloom sank out. The highest C_{remin} values were observed during blooms

of the picocyanobacteria *Synechococcus* in the first half of the study where oligotrophic conditions prevailed. Relatively high values were also observed during the mass flux event of a decaying diatom bloom although only in some mesocosms. The variability between mesocosms points toward additional but unknown factors driving C_{remin} of sinking material, which have yet to be revealed. Lowest C_{remin} values were measured during a HAB, suggesting that POC formed by toxic algae could be particularly efficient in transferring carbon into the deep ocean.

The efficiency of the BCP varies widely on spatial and temporal scales, but there is insufficient mechanistic understanding of the processes causing this variability so that export models show a wide range of predictive skill (Burd et al., 2016). A recent comparison of export flux observations in the subtropical Atlantic with predictions from state-of-the-art export models found that the one model including simple plankton interactions was better suited to predict regional variabilities in export fluxes than those lacking this aspect (Estapa et al., 2019). Our results strongly suggest that significant room for improvement of these ecosystem components lies in the parameterization of C_{remin} as a function of plankton community structure, as well as autotrophic to heterotrophic coupling. Thus, future studies should aim to include measurements of C_{remin} alongside plankton community structure to provide the mechanisms that lead to a more complete *predictive understanding* of the biological carbon pump.

References

Algueró-Muñiz, M., Horn, H. G., Alvarez-Fernandez, S., Spisla, C., Aberle, N., Bach, L. T., et al. (2019). Analyzing the impacts of elevated-CO$_2$ levels on the development of a subtropical zooplankton community during oligotrophic conditions and simulated upwelling. *Frontiers in Marine Science*, *6*(February), 1–18. https://doi.org/10.3389/fmars.2019.00061

Alldredge, A. L., & Gotschalk, C. (1988). In situ settling behavior of marine snow. *Limnology and Oceanography*, *33*(3), 339–351. https://doi.org/10.4319/lo.1988.33.3.0339

Armstrong, R. A., Lee, C., Hedges, J. I., Honjo, S., & Wakeham, S. G. (2002). A new, mechanistic model for organic carbon fluxes in the ocean based on the quantitative association of POC with ballast minerals. *Deep Sea Research Part II: Topical Studies in Oceanography*, *49*(1–3), 219–236.

Armstrong, R. A., Peterson, M. L., Lee, C., & Wakeham, S. G. (2009). Settling velocity spectra and the ballast ratio hypothesis. *Deep-Sea Research Part II: Topical Studies in Oceanography*, *56*(18), 1470–1478. https://doi.org/10.1016/j.dsr2.2008.11.032

Azetsu-Scott, K., & Passow, U. (2004). Ascending marine particles: Significance of transparent exopolymer particles (TEP) in the upper ocean. *Limnology and Oceanography*, *49*(3), 741–748. https://doi.org/10.4319/lo.2004.49.3.0741

Bach, L. T., Alvarez-Fernandez, S., Hornick, T., Stuhr, A., & Riebesell, U. (2017). Simulated ocean acidification reveals winners and losers in coastal phytoplankton. *Plos One*, *12*(11), e0188198. https://doi.org/10.1371/journal.pone.0188198

Bach, L. T., Boxhammer, T., Larsen, A., Hildebrandt, N., Schulz, K. G., & Riebesell, U. (2016). Influence of plankton community structure on the sinking velocity of marine aggregates. *Global Biogeochemical Cycles*, *30*, 1199–1214. https://doi.org/10.1002/2014GB004832

Bach, L. T., Lohbeck, K. T., Reusch, T. B. H., & Riebesell, U. (2018). Rapid evolution of highly variable competitive abilities in a key phytoplankton species. *Nature Ecology & Evolution*, *2*(4), 611–613. https://doi.org/10.1038/s41559-018-0474-x

Bach, L. T., Riebesell, U., Gutowska, M. A., Federwisch, L., & Schulz, K. G. (2015). A unifying concept of coccolithophore sensitivity to changing carbonate chemistry embedded in an ecological framework. *Progress in Oceanography*, *135*, 125–138. https://doi.org/10.1016/j.pocean.2015.04.012

Bach, L. T., Riebesell, U., Sett, S., Febiri, S., Rzepka, P., & Schulz, K. G. (2012). An approach for particle sinking velocity measurements in the 3–400 μm size range and considerations on the effect of temperature on sinking rates. *Marine Biology*, *159*(8), 1853–1864. https://doi.org/10.1007/s00227-012-1945-2

Belcher, A., Iversen, M., Manno, C., Henson, S. A., Tarling, G. A., & Sanders, R. (2016). The role of particle associated microbes in remineralization of fecal pellets in the upper mesopelagic of the Scotia Sea, Antarctica. *Limnology and Oceanography*, *61*(3), 1049–1064. https://doi.org/10.1002/lno.10269

Berelson, W. M. (2001). The flux of particulate organic carbon into the ocean interior: A comparison of four U.S. JGOFS regional studies. *Oceanography*, *14*(4), 59–67. https://doi.org/10.5670/oceanog.2001.07

Berggren, M., Lapierre, J. F., & Del Giorgio, P. A. (2012). Magnitude and regulation of bacterioplankton respiratory quotient across freshwater environmental gradients. *ISME Journal*, *6*(5), 984–993. https://doi.org/10.1038/ismej.2011.157

Boss, E., Guidi, L., Richardson, M. J., Stemmann, L., Gardner, W., Bishop, J. K. B., et al. (2015). Optical techniques for remote and in-situ characterization of particles pertinent to GEOTRACES. *Progress in Oceanography*, *133*, 43–54. https://doi.org/10.1016/j.pocean.2014.09.007

Boxhammer, T., Bach, L. T., Czerny, J., & Riebesell, U. (2016). Technical note: Sampling and processing of mesocosm sediment trap material for quantitative biogeochemical analysis. *Biogeosciences*, *12*(22), 18,693–18,722. https://doi.org/10.5194/bgd-12-18693-2015

Boxhammer, T., Taucher, J., Bach, L. T., Achterberg, E. P., Algueró-Muñiz, M., Bellworthy, J., et al. (2018). Enhanced transfer of organic matter to higher trophic levels caused by ocean acidification and its implications for export production: A mass balance approach. *PLoS ONE*, *13*(5), 1–25. https://doi.org/10.1371/journal.pone.0197502

Boyd, P. W. (2015). Toward quantifying the response of the oceans' biological pump to climate change. *Frontiers in Marine Science*, *2*(October), 1–15. https://doi.org/10.3389/fmars.2015.00077

Boyd, P. W., Claustre, H., Levy, M., Siegel, D. A., & Weber, T. (2019). Multi-faceted particle pumps drive carbon sequestration in the ocean. *Nature*, *568*(7752), 327–335. https://doi.org/10.1038/s41586-019-1098-2

Boyd, P. W., Mcdonnell, A., Valdez, J., Lefevre, D., & Gall, M. P. (2015). RESPIRE: An in situ particle interceptor to conduct particle remineralization and microbial dynamics studies in the oceans' twilight zone. *Limnology and Oceanography: Methods*, *13*(9), 494–508. https://doi.org/10.1002/lom3.10043

Boyd, P. W., & Trull, T. W. (2007). Understanding the export of biogenic particles in oceanic waters: Is there consensus? *Progress in Oceanography*, *72*(4), 276–312. https://doi.org/10.1016/j.pocean.2006.10.007

Bressac, M., Guieu, C., Doxaran, D., Bourrin, F., Desboeufs, K., Leblond, N., & Ridame, C. (2014). Quantification of the lithogenic carbon pump following a simulated dust-deposition event in large mesocosms. *Biogeosciences*, *11*(4), 1007–1020. https://doi.org/10.5194/bg-11-1007-2014

Buesseler, K. O. (1998). The decoupling of production and particulate export in the surface ocean. *Global Biogeochemical Cycles*, *12*(2), 297–310. https://doi.org/10.1029/97GB03366

Buesseler, K. O., & Boyd, P. W. (2009). Shedding light on processes that control particle export and flux attenuation in the twilight zone of the open ocean. *Limnology and Oceanography*, *54*(4), 1210–1232. https://doi.org/10.4319/lo.2009.54.4.1210

Burd, A. B., Buchan, A., Church, M., Landry, M., McDonnell, A., Passow, U., et al. (2016). Towards a transformative understanding of the ocean s biological pump: Priorities for future research. Report of the NSF Biology of the Biological Pump Workshop, February 19-20, 2016.

Burd, A. B., & Jackson, G. A. (2009). Particle aggregation. *Annual Review of Marine Science*, *1*(1), 65–90. https://doi.org/10.1146/annurev.marine.010908.163904

Cavan, E. L., & Boyd, P. W. (2018). Effect of anthropogenic warming on microbial respiration and particulate organic carbon export rates in the sub-Antarctic Southern Ocean. *Aquatic Microbial Ecology*, *82*(2), 111–127. https://doi.org/https://doi.org/10.3354/ame01889

Cavan, E. L., Trimmer, M., Shelley, F., & Sanders, R. (2017). Remineralization of particulate organic carbon in an ocean oxygen minimum zone. *Nature Communications*, *8*(1). https://doi.org/10.1038/ncomms14847

Chang, F. H., McVeagh, M., Gall, M., & Smith, P. (2012). *Chattonella globosa* is a member of Dictyochophyceae: Reassignment to *Vicicitus* gen. nov., based on molecular phylogeny, pigment composition, morphology and life history. *Phycologia*, *51*(4), 403–420. https://doi.org/10.2216/10-104.1

Chisholm, S. W. (1992). Phytoplankton size. In P. G. Falkowski, A. Woodhead, & K. Vivirito (Eds.), *Primary productivity and biogeochemical cycles in the sea*, (pp. 213–237). Boston: Springer. https://doi.org/10.1007/978-1-4899-0762-2

Chu, C. P., Lee, D. J., & Peng, X. F. (2004). Structure of conditioned sludge flocs. *Water Research*, *38*(8), 2125–2134. https://doi.org/10.1016/j.watres.2004.02.003

Cisternas-Novoa, C., Lee, C., & Engel, A. (2015). Transparent exopolymer particles (TEP) and Coomassie stainable particles (CSP): Differences between their origin and vertical distributions in the ocean. *Marine Chemistry*, *175*, 56–71. https://doi.org/10.1016/j.marchem.2015.03.009

Collins, J. R., Edwards, B. R., Thamatrakoln, K., Ossolinski, J. E., DiTullio, G. R., Bidle, K. D., et al. (2015). The multiple fates of sinking particles in the North Atlantic Ocean. *Global Biogeochemical Cycles*, *29*, 1471–1494. https://doi.org/10.1002/2014GB005037

De La Rocha, C. L., & Passow, U. (2007). Factors influencing the sinking of POC and the efficiency of the biological carbon pump. *Deep Sea Research Part II: Topical Studies in Oceanography*, *54*(5-7), 639–658. https://doi.org/10.1016/j.dsr2.2007.01.004

Ducklow, H. W., Steinberg, D. K., & Buesseler, K. O. (2001). Upper ocean carbon export and the biological pump. *Oceanography*, *14*(4), 50–58. https://doi.org/10.5670/oceanog.2001.06

Engel, A., & Schartau, M. (1999). Influence of transparent exopolymer particles (TEP) on sinking velocity of *Nitzschia closterium* aggregates. *Marine Ecology Progress Series*, *182*, 69–76. https://doi.org/10.3354/meps182069

Engel, A., Szlosek, J., Abramson, L., Liu, Z., & Lee, C. (2009). Investigating the effect of ballasting by $CaCO_3$ in *Emiliania huxleyi*: I. Formation, settling velocities and physical properties of aggregates. *Deep-Sea Research Part II: Topical Studies in Oceanography*, *56*(18), 1396–1407. https://doi.org/10.1016/j.dsr2.2008.11.027

Estapa, M. L., Feen, M. L., & Breves, E. (2019). Direct observations of biological carbon export from profiling floats in the subtropical North Atlantic. *Global Biogeochemical Cycles*, *33*, 282–300. https://doi.org/10.1029/2018GB006098

Field, C. B., Behrenfeld, M. J., Randerson, J. T., & Falkowski, P. G. (1998). Primary production of the biosphere: Integrating terrestrial and oceanic components. *Science*, *281*(5374), 237–240. https://doi.org/10.1126/science.281.5374.237

Fischer, G., & Karakaş, G. (2009). Sinking rates and ballast composition of particles in the Atlantic Ocean: Implications for the organic carbon fluxes to the deep ocean. *Biogeosciences*, *6*(1), 85–102. https://doi.org/10.5194/bg-6-85-2009

Flintrop, C. M., Rogge, A., Miksch, S., Thiele, S., Waite, A. M., & Iversen, M. H. (2018). Embedding and slicing of intact in situ collected marine snow. *Limnology and Oceanography: Methods*, *16*(6), 339–355. https://doi.org/10.1002/lom3.10251

Francois, R., Honjo, S., Krishfield, R., & Manganini, S. (2002). Factors controlling the flux of organic carbon to the bathypelagic zone of the ocean. *Global Biogeochemical Cycles*, *16*(4), 1087. https://doi.org/10.1029/2001GB001722

Gazeau, F., Sallon, A., Pitta, P., Tsiola, A., Maugendre, L., Giani, M., et al. (2017). Limited impact of ocean acidification on phytoplankton community structure and carbon export in an oligotrophic environment: Results from two short-term mesocosm studies in the Mediterranean Sea. *Estuarine, Coastal and Shelf Science*, *186*, 72–88. https://doi.org/10.1016/j.ecss.2016.11.016

Gelado-Caballero, M. D., López-García, P., Prieto, S., Patey, M. D., Collado, C., & Hérnndez-Brito, J. J. (2012). Long-term aerosol measurements in Gran Canaria, Canary Islands: Particle concentration, sources and elemental composition. *Journal of Geophysical Research*, *117*, D03304. https://doi.org/10.1029/2011JD016646

Giering, S. L. C., Sanders, R., Martin, A. P., Henson, S. A., Riley, J. S., Marsay, C. M., & Johns, D. G. (2017). Particle flux in the oceans: Challenging the steady state assumption. *Global Biogeochemical Cycles*, *31*, 159–171. https://doi.org/10.1002/2016GB005424

Goldthwait, S. A., Carlson, C. A., Henderson, G. K., & Alldredge, A. L. (2005). Effects of physical fragmentation on remineralization of marine snow. *Marine Ecology Progress Series*, *305*, 59–65. https://doi.org/10.3354/meps305059

Guidi, L., Jackson, G. A., Stemmann, L., Miquel, J. C., Picheral, M., & Gorsky, G. (2008). Relationship between particle size distribution and flux in the mesopelagic zone. *Deep-Sea Research Part I: Oceanographic Research Papers*, *55*(10), 1364–1374. https://doi.org/10.1016/j.dsr.2008.05.014

Guidi, L., Legendre, L., Reygondeau, G., Uitz, J., Stemmann, L., & Henson, S. A. (2015). A new look at the ocean carbon remineralization for estimating deepwater sequestration. *Global Biogeochemical Cycles*, *29*, 1044–1059. https://doi.org/10.1002/2014GB005063

Guidi, L., Stemmann, L., Jackson, G. A., Ibanez, F., Claustre, H., Legendre, L., et al. (2009). Effects of phytoplankton community on production, size and export of large aggregates: A world-ocean analysis. *Limnology and Oceanography*, *54*(6), 1951–1963. https://doi.org/10.4319/lo.2009.54.6.1951

Hansell, D. A., & Carlson, C. A. (2001). Marine dissolved organic matter and the carbon cycle. *Oceanography*, *14*(4), 41–49. https://doi.org/10.5670/oceanog.2001.05

Hansen, H. P., & Koroleff, F. (1999). Determination of nutrients. In K. Grasshoff, K. Kremling, & M. Ehrhardt (Eds.), *Methods of Seawater Analysis*, (pp. 159–226). Weinheim: Wiley-VCH. https://doi.org/10.1002/9783527613984.ch10

Henson, S., Lampitt, R., & Johns, D. (2012). Variability in phytoplankton community structure in response to the North Atlantic Oscillation and implications for organic carbon flux. *Limnology and Oceanography*, *57*(6), 1591–1601. https://doi.org/10.4319/lo.2012.57.6.1591

Henson, S. A., Sanders, R., & Madsen, E. (2012). Global patterns in efficiency of particulate organic carbon export and transfer to the deep ocean. *Global Biogeochemical Cycles*, *26*, GB1028. https://doi.org/10.1029/2011GB004099

Henson, S. A., Sanders, R., Madsen, E., Morris, P. J., Le Moigne, F., & Quartly, G. D. (2011). A reduced estimate of the strength of the ocean's biological carbon pump. *Geophysical Research Letters*, *38*, L04606. https://doi.org/10.1029/2011GL046735

Henson, S. A., Yool, A., & Sanders, R. (2015). Variability in efficiency of particulate organic carbon export: A model study. *Global Biogeochemical Cycles*, *29*, 33–45. https://doi.org/10.1002/2014GB004965.Received

Hernández-León, S., Putzeys, S., Almeida, C., Bécognée, P., Marrero-Díaz, A., Arístegui, J., & Yebra, L. (2019). Carbon export through zooplankton active flux in the Canary Current. *Journal of Marine Systems*, *189*, 12–21. https://doi.org/10.1016/j.jmarsys.2018.09.002

Herndl, G. J., & Reinthaler, T. (2013). Microbial control of the dark end of the biological pump. *Nature Geoscience*, *6*(9), 718–724. https://doi.org/10.1038/ngeo1921

van Heukelem, L., & Thomas, C. S. (2001). Computer-assisted high-performance liquid chromatography method development with applications to the isolation and analysis of phytoplankton pigments. *Jouranl of Chromatography A*, *910*(1), 31–49. https://doi.org/10.1016/S0378-4347(00)00603-4

Holmes, R. M., Aminot, A., Kérouel, R., Hooker, B. A., & Peterson, B. J. (1999). A simple and precise method for measuring ammonium in marine and freshwater ecosystems. *Canadian Journal of Fisheries and Aquatic Sciences*, *56*(10), 1801–1808. https://doi.org/10.1139/f99-128

Holtappels, M., Tiano, L., Kalvelage, T., Lavik, G., Revsbech, N. P., & Kuypers, M. M. M. (2014). Aquatic respiration rate measurements at low oxygen concentrations. *PloS One*, *9*(2), e89369. https://doi.org/10.1371/journal.pone.0089369

Honjo, S., Manganini, S. J., Krishfield, R. a., & Francois, R. (2008). Particulate organic carbon fluxes to the ocean interior and factors controlling the biological pump: A synthesis of global sediment trap programs since 1983. *Progress in Oceanography*, *76*(3), 217–285. https://doi.org/10.1016/j.pocean.2007.11.003

Iversen, M. H., Nowald, N., Ploug, H., Jackson, G. A., & Fischer, G. (2010). High resolution profiles of vertical particulate organic matter export off Cape Blanc, Mauritania: Degradation processes and ballasting effects. *Deep-Sea Research Part I: Oceanographic Research Papers*, *57*(6), 771–784. https://doi.org/10.1016/j.dsr.2010.03.007

Iversen, M. H., Pakhomov, E. A., Hunt, B. P. V., van der Jagt, H., Wolf-Gladrow, D., & Klaas, C. (2017). Sinkers or floaters? Contribution from salp pellets to the export flux during a large bloom event in the Southern Ocean. *Deep Sea Research Part II: Topical Studies in Oceanography*, *138*(December 2016), 116–125. https://doi.org/10.1016/j.dsr2.2016.12.004

Iversen, M. H., & Ploug, H. (2010). Ballast minerals and the sinking carbon flux in the ocean: Carbon-specific respiration rates and sinking velocity of marine snow aggregates. *Biogeosciences*, *7*(9), 2613–2624. https://doi.org/10.5194/bg-7-2613-2010

Iversen, M. H., & Ploug, H. (2013). Temperature effects on carbon-specific respiration rate and sinking velocity of diatom aggregates—Potential implications for deep ocean export processes. *Biogeosciences*, *7*(11ddd), 4073–4085. https://doi.org/10.1371/journal.pone.0049895

Kiørboe, T., Tiselius, P., Mitchell-Innes, B., Hansen, J. L. S., Visser, A. W., & Mari, X. (1998). *Limnology and Oceanography*, *43*(1), 104–116. https://doi.org/10.4319/lo.1998.43.1.0104

Klaas, C., & Archer, D. E. (2002). Association of sinking organic matter with various types of mineral ballast in the deep sea: Implications for the rain ratio. *Global Biogeochemical Cycles*, *16*(4), 1116. https://doi.org/10.1029/2001GB001765

Knapp, A. N., Fawcett, S. E., Martinez-Garcia, A., Leblond, N., Moutin, T., & Bonnet, S. (2016). Nitrogen isotopic evidence for a shift from nitrate- to diazotroph-fueled export production in the VAHINE mesocosm experiments. *Biogeosciences*, *13*(16), 4645–4657. https://doi.org/10.5194/bg-13-4645-2016

Kwon, E. Y., Primeau, F., & Sarmiento, J. L. (2009). The impact of remineralization depth on the air–sea carbon balance. *Nature Geoscience*, *2*(9), 630–635. https://doi.org/10.1038/ngeo612

Lam, P. J., & Bishop, J. K. B. (2007). High biomass, low export regimes in the Southern Ocean. *Deep-Sea Research Part II: Topical Studies in Oceanography*, *54*(5-7), 601–638. https://doi.org/10.1016/j.dsr2.2007.01.013

Lam, P. J., Doney, S. C., & Bishop, J. K. B. (2011). The dynamic ocean biological pump: Insights from a global compilation of particulate organic carbon, CaCO$_3$, and opal concentration profiles from the mesopelagic. *Global Biogeochemical Cycles*, *25*, GB3009. https://doi.org/10.1029/2010GB003868

Laurenceau-Cornec, E. C., Trull, T. W., Davies, D. M., De La Rocha, C. L., & Blain, S. (2015). Phytoplankton morphology controls on marine snow sinking velocity. *Marine Ecology Progress Series*, *520*, 35–56. https://doi.org/10.3354/meps11116

Le Moigne, F. A. C., Cisternas-Novoa, C., Piontek, J., Maßmig, M., & Engel, A. (2017). On the effect of low oxygen concentrations on bacterial degradation of sinking particles. *Scientific Reports*, *7*(1), 1–12. https://doi.org/10.1038/s41598-017-16903-3

Le Moigne, F. A. C., Gallinari, M., Laurenceau, E., & De La Rocha, C. L. (2013). Enhanced rates of particulate organic matter remineralization by microzooplankton are diminished by added ballast minerals. *Biogeosciences*, *10*(9), 5755–5765. https://doi.org/10.5194/bg-10-5755-2013

Le Moigne, F. A. C., Henson, S. A., Cavan, E., Georges, C., Pabortsava, K., Achterberg, E. P., et al. (2016). What causes the inverse relationship between primary production and export efficiency in the Southern Ocean? *Geophysical Research Letters*, *43*, 4457–4466. https://doi.org/10.1002/2016GL068480

Legendre, L., Rivkin, R. B., & Jiao, N. (2018). Advanced experimental approaches to marine water-column biogeochemical processes. *ICES Journal of Marine Science*, *75*(1), 30–42. https://doi.org/10.1093/icesjms/fsx146

Leppard, G. G., Heissenberger, A., & Herndl, G. J. (1996). Ultrastructure of marine snow: I. Transmission electron microscopy methodology. *Marine Ecology Progress Series*, *135*(1–3), 289–298. https://doi.org/10.3354/meps135289

Lischka, S., Stange, P., & Riebesell, U. (2018). Response of pelagic calcifiers (Foraminifera, Thecosomata) to ocean acidification during oligotrophic and simulated up-welling conditions in the subtropical North Atlantic off Gran Canaria. *Frontiers in Marine Science*, *5*(October), 379. https://doi.org/10.3389/fmars.2018.00379

Logan, B. E., & Wilkinson, D. B. (1990). Fractal geometry of marine biological aggregates. *Limnology & Oceanography*, *35*(1), 130–136. https://doi.org/10.4319/lo.1990.35.1.0130

Lomas, M. W., Steinberg, D. K., Dickey, T., Carlson, C. A., Nelson, N. B., Condon, R. H., & Bates, N. R. (2010). Increased ocean carbon export in the Sargasso Sea is countered by its enhanced mesopelagic attenuation. *Biogeosciences*, *6*(5), 9547–9582. https://doi.org/10.5194/bgd-6-9547-2009

Lombard, F., da Rocha, R. E., Bijma, J., & Gattuso, J.-P. (2010). Effect of carbonate ion concentration and irradiance on calcification in planktonic foraminifera. *Biogeosciences*, *7*(1), 247–255. https://doi.org/10.5194/bg-7-247-2010

Longhurst, A., Sathyendranath, S., Platt, T., & Caverhill, C. (1995). An estimate of global primary production in the ocean from satellite radiometer data. *Journal of Plankton Research*, *17*(6), 1245–1271. https://doi.org/10.1093/plankt/17.6.1245

Lutz, M. J., Caldeira, K., Dunbar, R. B., & Behrenfeld, M. J. (2007). Seasonal rhythms of net primary production and particulate organic carbon flux to depth describe the efficiency of biological pump in the global ocean. *Journal of Geophysical Research*, *112*, C10011. https://doi.org/10.1029/2006JC003706

Maiti, K., Charette, M. A., Buesseler, K. O., & Kahru, M. (2013). An inverse relationship between production and export efficiency in the Southern Ocean. *Geophysical Research Letters*, *40*, 1557–1561. https://doi.org/10.1002/grl.50219

Mari, X. (2008). Does ocean acidification induce an upward flux of marine aggregates? *Biogeosciences*, *5*(4), 1023–1031. https://doi.org/10.5194/bg-5-1023-2008

Mari, X., Passow, U., Migon, C., Burd, A. B., & Legendre, L. (2017). Transparent exopolymer particles: Effects on carbon cycling in the ocean. *Progress in Oceanography*, *151*, 13–37. https://doi.org/10.1016/j.pocean.2016.11.002

Marsay, C. M., Sanders, R. J., Henson, S. A., Pabortsava, K., Achterberg, E. P., & Lampitt, R. S. (2015). Attenuation of sinking particulate organic carbon flux through the mesopelagic ocean. *Proceedings of the National Academy of Sciences of the United States of America*, *112*, 1089–1094. https://doi.org/10.1073/pnas.1415311112

Martin, J. H., Knauer, G. A., Karl, D. M., & Broenkow, W. W. (1987). VERTEX: Carbon cycling in the northeast Pacific. *Deep Sea Research Part A Oceanographic Research Papers*, *34*(2), 267–285. https://doi.org/10.1016/0198-0149(87)90086-0

Mcdonnell, A. M. P., Boyd, P. W., & Buesseler, K. O. (2015). Effects of sinking velocities and microbial respiration rates on the attentuation of particulate carbon fluxes through the mesopelagic zone. *Global Biogeochemical Cycles*, *29*, 175–193. https://doi.org/10.1002/2013GB004679

McNown, J., & Malaika, J. (1950). Effects of particle shape on settling velocity at low Reynolds numbers. *Transactions of the American Geophysial Union*, *31*(1), 74–82. https://doi.org/10.1029/TR031i001p00074

Mouw, C. B., Barnett, A., Mckinley, G. A., Gloege, L., & Pilcher, D. (2016). Phytoplankton size impact on export flux in the global ocean. *Global Biogeochemical Cycles*, *30*, 1542–1562. https://doi.org/10.1002/2015GB005355

Mouw, C. B., Hardman-Mountford, N. J., Alvain, S., Bracher, A., Brewin, R. J. W., Bricaud, A., et al. (2017). A consumer's guide to satellite remote sensing of multiple phytoplankton groups in the global ocean. *Frontiers in Marine Science*, *4*(February). https://doi.org/10.3389/fmars.2017.00041

Murphy, J., & Riley, J. P. (1962). A modified single solution method for the determination of phosphate in natural waters. *Analytica Chimica Acta*, *27*, 31–36. https://doi.org/10.1016/S0003-2670(00)88444-5

Neuer, S., Torres-Padrón, M. E., Gelado-Caballero, M. D., Rueda, M. J., Hernández-Brito, J., Davenport, R., & Wefer, G. (2004). Dust deposition pulses to the eastern subtropical North Atlantic gyre: Does ocean's biogeochemistry respond? *Global Biogeochemical Cycles*, *18*, GB4020. https://doi.org/10.1029/2004GB002228

Nowald, N., Iversen, M. H., Fischer, G., Ratmeyer, V., & Wefer, G. (2015). Time series of in-situ particle properties and sediment trap fluxes in the coastal upwelling filament off Cape Blanc, Mauritania. *Progress in Oceanography*, *137*, 1–11. https://doi.org/10.1016/j.pocean.2014.12.015

Passow, U., & Alldredge, A. L. (1995). A dye-binding assay for the spectrophotometric measurement of transparent exopolymer particles (TEP). *Limnology and Oceanography*, *40*(7), 1326–1335. https://doi.org/10.4319/lo.1995.40.7.1326

Passow, U., & De La Rocha, C. L. (2006). Accumulation of mineral ballast on organic aggregates. *Global Biogeochemical Cycles*, *20*, GB1013. https://doi.org/10.1029/2005GB002579

Piontek, J., Lunau, M., Händel, N., Borchard, C., Wurst, M., & Engel, A. (2010). Acidification increases microbial polysaccharide degradation in the ocean. *Biogeosciences*, *7*(5), 1615–1624. https://doi.org/10.5194/bg-7-1615-2010

Ploug, H., & Bergkvist, J. (2015). Oxygen diffusion limitation and ammonium production within sinking diatom aggregates under hypoxic and anoxic conditions. *Marine Chemistry*, *176*, 142–149. https://doi.org/10.1016/j.marchem.2015.08.012

Ploug, H., & Grossart, H.-P. (2000). Bacterial growth and grazing on diatom aggregates: Respiratory carbon turnover as a function of aggregate size and sinking velocity. *Limnology & Oceanography*, *45*(7), 1467–1475. https://doi.org/10.4319/lo.2000.45.7.1467

Ploug, H., Grossart, H.-P., Azam, F., & Joergensen, B. B. (1999). Photosynthesis, respiration, and carbon turnover in sinking marine snow from surface waters of Southern California Bight: Implications for the carbon cycle in the ocean. *Marine Ecology Progress Series*, *179*, 1–11. https://doi.org/10.3354/meps179001

Ploug, H., Iversen, M. H., & Fischer, G. (2008). Ballast, sinking velocity, and apparent diffusivity within marine snow and zooplankton fecal pellets: Implications for substrate turnover by attached bacteria. *Limnology and Oceanography*, *53*(5), 1878–1886. https://doi.org/10.4319/lo.2008.53.5.1878

Prahl, F. G., Dymond, J., & Sparrow, M. A. (2000). Annual biomarker record for export production in the central Arabian Sea. *Deep-Sea Research Part II: Topical Studies in Oceanography*, *47*(7–8), 1581–1604. https://doi.org/10.1016/S0967-0645(99)00155-1

Puigcorbé, V., Benitez-Nelson, C. R., Masqué, P., Verdeny, E., White, A. E., Popp, B. N., et al. (2015). Small phytoplankton drive high summertime carbon and nutrient export in the Gulf of California and Eastern Tropical North Pacific. *Global Biogeochemical Cycles*, *29*, 397–415. https://doi.org/10.1002/2014GB004979

Riebesell, U., Aberle-Malzahn, N., Achterberg, E. P., Algueró-Muñiz, M., Alvarez-Fernandez, S., Arístegui, J., et al. (2018). Toxic algal bloom induced by ocean acidification disrupts the pelagic food web. *Nature Climate Change*, *8*(12), 1082–1086. https://doi.org/10.1038/s41558-018-0344-1

Riebesell, U., Czerny, J., von Bröckel, K., Boxhammer, T., Büdenbender, J., Deckelnick, M., et al. (2013). Technical note: A mobile sea-going mesocosm system—New opportunities for ocean change research. *Biogeosciences*, *10*(3), 1835–1847. https://doi.org/10.5194/bg-10-1835-2013

Robinson, C., & Williams, P. J. L. B. (1999). Plankton net community production and dark respiration in the Arabian Sea during September 1994. *Deep-Sea Research Part II: Topical Studies in Oceanography*, *46*(3–4), 745–765. https://doi.org/10.1016/S0967-0645(98)00126-X

Sanders, R., Henson, S. A., Koski, M., de la Rocha, C. L., Painter, S. C., Poulton, A. J., et al. (2014). The biological carbon pump in the North Atlantic. *Progress in Oceanography*, *129*, 200–218. https://doi.org/10.1016/j.pocean.2014.05.005

Sarmiento, J. L., & Gruber, N. (2006). *Ocean biogeochemical dynamics*. Princeton: Princeton University Press.

Schmidt, K., De La Rocha, C. L., Gallinari, M., & Cortese, G. (2014). Not all calcite ballast is created equal: Differing effects of foraminiferan and coccolith calcite on the formation and sinking of aggregates. *Biogeosciences*, *11*(1), 135–145. https://doi.org/10.5194/bg-11-135-2014

Schmittner, A., Oschlies, A., Matthews, H. D., & Galbraith, E. D. (2008). Future changes in climate, ocean circulation, ecosystems, and biogeochemical cycling simulated for a business-as-usual CO_2 emission scenario until year 4000 AD. *Global Biogeochemical Cycles*, *22*, GB1013. https://doi.org/10.1029/2007GB002953

Sharp, J. H. (1974). Improved analysis for "particulate" organic carbon and nitrogen from seawater. *Limnology and Oceanography*, *19*(6), 984–989. https://doi.org/10.4319/lo.1974.19.6.0984

Siegel, D. A., Buesseler, K. O., Doney, S. C., Sailley, S. F., Behrenfeld, M. J., & Boyd, P. W. (2014). Global assessment of ocean carbon export by combining satellite observations and food-web models. *Global Biogeochemical Cycles*, *28*, 181–196. https://doi.org/10.1002/2013GB004743

Stange, P., Bach, L. T., Le Moigne, F. A. C., Taucher, J., Boxhammer, T., & Riebesell, U. (2017). Quantifying the time lag between organic matter production and export in the surface ocean: Implications for estimates of export efficiency. *Geophysical Research Letters*, *44*, 268–276. https://doi.org/10.1002/2016GL070875

Stange, P., Taucher, J., Bach, L. T., Algueró-Muñiz, M., Horn, H. G., Krebs, L., et al. (2018). Ocean acidification-induced restructuring of the plankton food web can influence the degradation of sinking particles. *Frontiers in Marine Science*, *5*, 1–13. https://doi.org/10.3389/fmars.2018.00140

Steinberg, D. K., & Landry, M. R. (2017). Zooplankton and the ocean carbon cycle. *Annual Review of Marine Science*, *9*(1), 413–444. https://doi.org/10.1146/annurev-marine-010814-015924

Steinberg, D. K., Van Mooy, B. A. S., Buesseler, K. O., Boyd, P. W., Kobari, T., & Karl, D. M. (2008). Bacterial vs. zooplankton control of sinking particle flux in the ocean's twilight zone. *Limnology and Oceanography*, *53*(4), 1327–1338. https://doi.org/10.4319/lo.2008.53.4.1327

Stemmann, L., & Boss, E. (2012). Plankton and particle size and packaging: From determining optical properties to driving the biological pump. *Annual Review of Marine Science*, *4*(1), 263–290. https://doi.org/10.1146/annurev-marine-120710-100853

Stukel, M. R., Song, H., Goericke, R., & Miller, A. J. (2018). The role of subduction and gravitational sinking in particle export, carbon sequestration, and the remineralization length scale in the California Current Ecosystem. *Limnology and Oceanography*, *63*(1), 363–383. https://doi.org/10.1002/lno.10636

Taucher, J., Arístegui, J., Bach, L. T., Guan, W., Montero, M. F., Nauendorf, A., et al. (2018). Response of subtropical phytoplankton communities to ocean acidification under oligotrophic conditions and during nutrient fertilization. *Frontiers in Marine Science*, *5*(September), 1–14. https://doi.org/10.3389/fmars.2018.00330

Taucher, J., Bach, L. T., Boxhammer, T., Nauendorf, A., Achterberg, E. P., Algueró-Muñiz, M., et al., & The Gran Canaria KOSMOS Consortium (2017). Influence of ocean acidification and deep water upwelling on oligotrophic plankton communities in the subtropical North Atlantic: Insights from an in situ mesocosm study. *Frontiers in Marine Science*, *4*(85), 1–18. https://doi.org/10.3389/fmars.2017.00085

Taucher, J., Stange, P., Algueró-Muñiz, M., Bach, L. T., Nauendorf, A., Kolzenburg, R., et al. (2018). In situ camera observations reveal major role of zooplankton in modulating marine snow formation during an upwelling-induced plankton bloom. *Progress in Oceanography*, *164*(January), 75–88. https://doi.org/10.1016/j.pocean.2018.01.004

Utermöhl, T. (1958). Zur Vervollkommnung der quantitativen Phytoplankton-Methodik. *Vereinigung Für Theoretische Und Angewandte Limnologie*, *9*, 1–38.

Veldhuis, M. J. W., & Kraay, G. W. (2000). Application of flow cytometry in marine phytoplankton research: Current applications and future perspectives. *Scientia Marina*, *64*(2), 121–134. https://doi.org/10.3989/scimar.2000.64n2121

Volk, T., & Hoffert, M. I. (1985). Ocean carbon pumps: Analysis of relative strengths and efficiencies in ocean-driven atmospheric CO_2 changes. In E. T. Sundquist, & W. S. Broecker (Eds.), *The carbon cycle and atmospheric CO2: Natural variations Archean to present*, *Geophysica*, (Vol. 32, pp. 99–110). Washington D. C. https://doi.org/10.1029/GM032p0099

Ward, B. A., Dutkiewicz, S., Jahn, O., & Follows, M. J. (2012). A size-structured food-web model for the global ocean. *Limnology and Oceanography*, *57*(6), 1877–1891. https://doi.org/10.4319/lo.2012.57.6.1877

Weber, T., Cram, J. A., Leung, S. W., DeVries, T., & Deutsch, C. (2016). Deep ocean nutrients imply large latitudinal variation in particle transfer efficiency. *Proceedings of the National Academy of Sciences*, *113*(31), 8606–8611. https://doi.org/10.1073/pnas.1604414113

Wilson, J. D., Barker, S., & Ridgwell, A. (2012). Assessment of the spatial variability in particulate organic matter and mineral sinking fluxes in the ocean interior: Implications for the ballast hypothesis. *Global Biogeochemical Cycles*, *26*, GB4011. https://doi.org/10.1029/2012GB004398